

Target thickness studies, run 1 - E06007

Konrad A. Aniol, CSULA

March 10, 2011

Contents

1	Synopsis	8
2	Initial Target Configurations	10
3	Introduction	13
3.1	Counting rate and target/beam morphology	14
4	Graphite data	16
5	Graphite results	21
6	GEANT simulations of carbon spectrum in lead	24
7	Lead data	30
7.1	Lead data	30
7.2	Lead target pb4	36
7.3	Lead discussion	38
7.4	Kinematics 12 and 13	39
8	Lead Results	48
8.1	Kinematics 1-11	48
8.2	Kinematics 12 and 13	48
9	Bismuth data	54
9.1	Bismuth Data	54
9.2	Bismuth Results	57

List of Tables

1.1	Effective target thicknesses based on LHRS singles yields. The effective thickness is determined from the average yield using equation 7.1. A * indicates reversed raster currents. Radiative corrections have been applied to the subtracted carbon spectrum. Raster changed between kin07a and kin07b, see table 7.11. Raster changed during kin09a,b,c, see table 7.13.	9
1.2	Bismuth effective target thicknesses based on LHRS singles yields. The effective thickness is determined from the average yield using equation 7.1. A * indicates reversed raster currents. The bismuth effective thickness includes an additional factor of 82/83 to account for the extra proton in bismuth compared to lead and a factor of 1.04 to account for radiative differences.	9
2.1	Run 1, March 2007, diamond foils as per Phil Adderley, email June 12, 2008.	11
2.2	Run 1, March 2007, from Dave Meekins, February 27,2007. Target ladder is tilted at 30 degrees.	11
2.3	Run 2, January, 2008 from top to bottom. Targets are 1"x1", per Phil Adderley and Dave Meekins.	12
4.1	Quantities in the spreadsheet used to determine number of nuclei in the beam.	17
4.2	Normalized LHRS singles counts for rastered and unrastered beam for the graphite target. Raster leads in the correct configuration. Average singles rastered yield for $\theta_L = 21.44^\circ$ is $4.83 \pm 0.17 \times 10^7$. *For kin12 and kin13 the LHRS was moved to new angles and central momenta.	18
4.3	Normalized LHRS singles counts for rastered beam for the graphite target. Raster leads are in the inverted configuration but raster correction for normal lead configuration was used. Average singles yield = $5.11 \pm 0.08 \times 10^7$	18

6.1	Momenta and angles for the LHRS. The rad. loss factor is to be multiplied against the normalized graphite yield to account for radiative losses of events from the diamond foils due to the heavy metal foil.	25
7.1	kin01-Normalized LHRS singles counts for the pb3 target. Normal raster currents. raster pattern r1518, A(.006,.0023),B(.0134,.0101), cutsx(.007,.011),cutsy(.003,.009)	30
7.2	kin01-Normalized LHRS singles counts for the pb3 target. Reversed raster currents. raster pattern r1723, A(.0061,.0028),B(.0134,.0098), cutsx(.007,.011),cutsy(.003,.009)	31
7.3	kin02-Normalized LHRS singles counts for the pb3 target. raster pattern r1731, A(.0060,0.0028),B(.0135,.0098),cutsx (.007,.011),cutsy(0.004,.009). Reversed raster currents.	31
7.4	kin03-Normalized LHRS singles counts for the pb3 target. raster pattern r1645, A(.006,.0028),B(.0135,.0098), cutsx(.007,.011),cutsy(.003,.009)	31
7.5	kin04-Normalized LHRS singles counts for the pb3 target. Normal raster currents. raster pattern r1339, A(.005,.003),B(.014,.0095), cutsx(.007,.012),cutsy(.004,.009), raster fraction = 0.513.	32
7.6	kin04-Normalized LHRS singles counts for the pb3 target. Normal raster currents. raster pattern r1339, A(.005,.003),B(.014,.0095), cutsx(.007,.012),cutsy(.004,.009), raster fraction = 0.256.	32
7.7	kin04-Normalized LHRS singles counts for the pb3 target. reversed raster currents. raster pattern r1339, A(.005,.003),B(.014,.0095), cutsx(.007,.012),cutsy(.004,.009)	32
7.8	kin05-Normalized LHRS singles counts for the pb3 target. Mixed raster currents. raster pattern r1610, A(.006,.0028),B(.0135,.0098), cutsx(.007,.012),cutsy(.004,.009). run no.* means reversed raster currents.	33
7.9	kin06-Normalized LHRS singles counts for the pb3 target. raster pattern r1419, A(.006,.0023),B(.01345,.01), cutsx(.007,.011),cutsy(.004,.009). 33	
7.10	kin06-Normalized LHRS singles counts for the pb3 target. reversed raster currents. raster pattern r1917, A(.0054,.0037),B(.0140,.0089), cutsx(.007,.012),cutsy(.0045,.0075).	33
7.11	kin07-Normalized LHRS singles counts for the pb3 target. raster pattern r1541, A(.006,.0022),B(.0135,.01), cutsx(.007,.011),cutsy(.003,.009). *changed raster pattern r1596 A(x,y)=(0.0060,0.0028),B(0.0135,0.0098), cutsx(.007,.011),cutsy(.003,.009).	34
7.12	kin08-Normalized LHRS singles counts for the pb3 target. Reversed raster currents. raster pattern r1689, A(0.006,0.0028),B(.0135,0.0098), cutsx(0.007,0.011),cutsy(0.004,0.009)	34

7.13	kin09-Normalized LHRS singles counts for the pb3 target. Reversed raster currents. r1859,A(0.0054,0.0035),B(0.0139,0.0091),cutsx(0.007,0.013),cutsy(0.0045,0.008),*r1873, A(0.0055,0.0037),B(0.0139,0.0088),cutsx(0.007,0.013),cutsy(0.0045,0.008):**r1889, A(0.0062,0.0034),B(0.0132,0.009),cutsx(0.007,0.013),cutsy(0.0045,0.008)	35
7.14	kin10-Normalized LHRS singles counts for the pb3 target. Reversed raster currents. raster pattern r1773,A(0.006,0.003), B(0.0135,0.0095), cutsx(0.007,0.012),cutsy(0.004,0.008).	36
7.15	kin11-Normalized LHRS singles counts for the pb3 target. Reversed raster currents. raster pattern. r1895, A(0.0055,0.0037),B(0.0139,0.0088),cutsx(0.007,0.013),cut	36
7.16	kin11-Normalized LHRS singles counts for the pb3 target. Reversed raster currents. raster pattern. r1895, A(0.0055,0.0037),B(0.0139,0.0088),cutsx(0.007,0.013),cut	37
7.17	kin01-Normalized LHRS singles counts for the pb4 target. Normal raster currents. raster pattern from r1215 A(0.0004,-0.0022),B(0.0105,0.0065),cutsx(0.001,0.008),c	37
7.18	kin02-Normalized LHRS singles counts for the pb4 target. Normal raster currents. raster pattern r1231, A(.00030,-.0022),B(.0105,.0065),cutsx(0.001,0.007),cutsy(-0.001,0.005). *raster pattern changed from r1255 onward, A(0.0048,0.0003),B(0.0215,0.0159),cutsx(0.007,0.020),cutsy(0.002,0.014).	38
7.19	kin12-Normalized LHRS singles counts for the pb3 target. Normal raster currents. raster pattern r1506, A(.006,0.0022),B(.0135,0.0104),cutsx(0.007,0.011),cutsy(0.004,0.009).	39
7.20	kin13-Normalized LHRS singles counts for the pb3 target. Normal raster currents. raster pattern r1491, A(.006,0.0022),B(.0135,0.0104),cutsx(0.007,0.011),cutsy(0.004,0.009).	39
8.1	Effective target thicknesses based on LHRS singles yields. Radiative corrections have been applied to the carbon subtracted spectrum. The effective thickness is determined from the average yield using equation 7.1. A * indicates reversed raster currents. Raster changed between kin07a and kin07b, see table 7.11. Raster changed during kin09a,b,c, see table 7.13.	49
8.2	Target Pb4. Effective target thicknesses based on LHRS singles yields. Radiative corrections have been applied to the carbon subtracted spectrum. The effective thickness is determined from the average yield using equation 7.1. Raster changed between kin02a and kin02b, see table 7.18.	49
8.3	Effective target thicknesses based on LHRS singles yields. No radiative correction to the carbon subtracted spectrum have been applied. The effective thickness is determined from the average yield using equation 7.1 with the normalization yield = 8.177×10^7 . A * indicates reversed raster currents. Raster changed between kin07a and kin07b, see table 7.11. Raster changed during kin09a,b,c, see table 7.13.	50

8.4	Target Pb4. Effective target thicknesses based on LHRS singles yields. No radiative correction to the carbon subtracted spectrum have been applied. The effective thickness is determined from the average yield using equation 7.1 with the normalization yield = 8.177×10^7 . Raster changed between kin02a and kin02b, see table 7.18.	50
8.5	The ratio yield(pb)/yield(c) for momenta and angles for the LHRS. 51	
9.1	kin02-Normalized LHRS singles counts for the bismuth target. Normal raster curenents. raster pattern r1326, A(.0051,.003),B(.0143,.0095), cutsx(.006,.013),cutsy(.006,.0085)	57
9.2	kin03-Normalized LHRS singles counts for the bismuth target. Reverse raster curenents. raster pattern r1977, A(.0055,.0037),B(.0140,.0088), cutsx(.0095,.013),cutsy(.005,.008)	57
9.3	kin04-Normalized LHRS singles counts for the bismuth target. Normal raster curenents. raster pattern r1360, A(.006,.0022),B(.0134,.0102), cutsx(.007,.012),cutsy(.006,.009)	58
9.4	kin04-Normalized LHRS singles counts for the bismuth target. Reverse raster curenents. raster pattern r1960, A(.0054,.0037),B(.0140,.0088), cutsx(.009,.013),cutsy(.005,.008)	58
9.5	kin05-Normalized LHRS singles counts for the bismuth target. Reverse raster curenents. raster pattern r1985 A(0.0055,0.0037),B(0.014,0.0088),cutsx(0.01,0.013),cutsy(0.01,0.013)	58
9.6	kin06-Normalized LHRS singles counts for the bismuth target. normal raster curenents. raster pattern. r1422, A(0.006,0.0023), B(0.0135,0.010),cutsx(0.007,0.012),cutsy(0.006,0.009).	59
9.7	kin07-Normalized LHRS singles counts for the bismuth target. reverse raster curenents. raster pattern. r2008 A(0.0055,0.0037),B(0.014,0.0088),cutsx(0.01,0.013),cutsy(0.01,0.013)	59
9.8	Bismuth effective target thicknesses based on LHRS singles yields. Radiative corrections to the subtracted carbon spectrum have been applied. The effective thickness is determined from the average yield using equation 7.1. A * indicates reversed raster currents. The bismuth effective thickness includes an additional factor of 82/83 to account for the extra proton in bismuth compared to lead and a factor of 1.04 to account for radiative differences.	60
9.9	Bismuth effective target thicknesses based on LHRS singles yields. No radiative corrections to the subtracted carbon spectrum have been applied. The effective thickness is determined from the average yield using equation 7.1 for a normalization factor of 8.177×10^7 . A * indicates reversed raster currents. The bismuth effective thickness includes an additional factor of 82/83 to account for the extra proton in bismuth compared to lead.	60

List of Figures

4.1	Sample of a raster pattern with typical cuts shown. Points A and B at the corners determine the total area of the raster, A_T . The rectangle shows the area A used in the LHRS cut to generate the singles spectrum.	19
4.2	Sample of a singles and coincidence momentum spectra in the LHRS with typical cuts.	20
5.1	Reaction point for run 1518. The matrix shows the areas of the raster patterned investigated to determine uniformity in count rate. Counts in the 20 small regions were tallied.	23
6.1	The solid curve is the measured graphite spectrum. The dashed curve shows the geant predicted spectrum. The two curves are normalized to each other at $dp = -0.03$ and were generated for the same number of electrons in the input file(the measured graphite spectrum).	26
6.2	The solid curve is the measured lead(pb3) spectrum. The dashed curve shows the measured graphite spectrum. The two curves are normalized to each other at $dp = -0.03$	27
6.3	The solid curve is the measured graphite spectrum for kinematics 12. The dashed curve shows the geant predicted spectrum after passing through the lead target.	28
6.4	The solid curve is the measured graphite spectrum for kinematics 13. The dashed curve shows the geant predicted spectrum after passing through the lead target.	29
7.1	A plot of ReactPt.L.x vs ReactPt.L.y of the lead target4, run 1215, for the first run of kin01. Depletion of lead is already seen here.	40
7.2	A plot of ReactPt.L.x vs ReactPt.L.y of the lead target4, run 1260, for kin02. The size of the depleted lead region is substantially larger than in figure 7.1.	41
7.3	A 3 dimensional plot of ReactPt.L.x vs ReactPt.L.y of the lead target3, run 1585, for kin07.	42

7.4	A 3 dimensional plot of ReactPt_L.x vs ReactPt_L.y of the lead target3, runs 1913,1914,1915 for kin11.	43
7.5	A 3 dimensional plot of ReactPt_L.x vs ReactPt_L.y of the lead target3, run 1609, for kin07.	44
7.6	A 3 dimensional plot of ReactPt_L.x vs ReactPt_L.y of the lead target3, runs 1376 to 1380 for kin04. These are low current runs($I \leq 10\mu\text{A}$) taken when pb3 was first placed in the beam.	45
7.7	Measured L.gold.dp for kinematics 12. The spectra are normalized to have the same number of counts.	46
7.8	Measured L.gold.dp for kinematics 13. The spectra are normalized to have the same number of counts.	47
8.1	Normalized yield vs run number. The vertical scale should be multiplied by 10^5	52
8.2	3D raster yield plot for runs 1928,1929,1930.	53
9.1	A 3 dimensional plot of ReactPt_L.x vs ReactPt_L.y of the bismuth target, run 1360, for kin04 showing the ragged topology of the metal surface and the bare diamond substrate.	55
9.2	A 3 dimensional plot of ReactPt_L.x vs ReactPt_L.y of the bismuth target, run 1960, for kin04 showing the ragged topology of the metal surface and the bare diamond substrate. The raster current leads were accidently switched.	56
9.3	A 3 dimensional plot of ReactPt_L.x vs ReactPt_L.y of the bismuth target, run 1326.	61
9.4	A plot of ReactPt_L.x vs ReactPt_L.y of the bismuth target, for the first 80000 events of run 1326. This is the first run of kin02. The damage to the target is already evident. The target started out damaged, probably during the Iscan runs.	62
9.5	A plot of trigger 3 rate versus current for the bismuth target taken prior to run 1326 during the Iscan run, hall A logbook entry 195299, March 9, 2007.	63

Chapter 1

Synopsis

Heavy metal target thicknesses are deduced from the left high resolution spectrometer (LHRS) singles spectra for run1 taken in March 2007 of E06007. The results of this study for lead target 3(pb3) are presented in table 8.1 and reproduced here in table 1.1. A systematic increase in the yield in the LHRS singles spectra, shown in figure 8.1 is consistent with a changing target morphology over the course of the run. The effective lead target density is based on the results of low current ($I \leq 10\mu A$) and is given by

$$\frac{6.51 \times 10^{20}/cm^2}{9.073 \times 10^7/Coulomb_{eff}} = \frac{effective\ pb\ thickness}{yield/Coulomb_{eff}} \quad (1.1)$$

The carbon contribution must be subtracted first from the diamond/lead target to use this equation. The results for the graphite target for the rastered beam yield per coulomb is $4.83 \pm 0.17 \times 10^7$, which is a 4% standard deviation in the assumed target thickness by the luminosity comparison. For the unrastered beam the yield per Coulomb is $5.19 \pm 0.05 \times 10^7$. The difference between unrastered and rastered beam is $5.19/4.83 = 1.07$ and hence we can not claim we know the target thickness to better than 7% from the graphite data. For runs beyond run 1624 when the raster leads were switched the yield per Coulomb is $5.11 \pm 0.08 \times 10^7$. The ratio of yields for the rastered beam is $4.83/5.11 = 0.95$ and this factor is used in table 1.1 to determine the target thickness after the raster lead switch.

Lead target 4(pb4) can also be used for kinematics 01 and 02. The effective thicknesses for this target for representative cuts are shown in table 8.2.

Effective thicknesses for the bismuth target are shown in table 9.8 and reproduced here in table 1.2. Target thicknesses for bismuth are first calculated as if the target were lead and the result is multiplied by a factor of 82/83 to account for the ratio of protons and by a factor of 1.04 to account for radiative effects to give the bismuth target density.

Details supporting these results follow.

kin	cutsx	cutsy	average yield $\times 10^7 / \text{Coulomb}$	normalization factor	effective thickness $\times 10^{20} / \text{cm}^2$
01	(0.007,0.011)	(0.003,0.009)	8.87 ± 0.01	1	6.37 ± 0.01
01*	(0.007,0.011)	(0.003,0.009)	8.20 ± 0.01	0.95	6.27 ± 0.01
02*	(0.007,0.011)	(0.004,0.009)	9.28 ± 0.01	0.95	6.33 ± 0.01
03*	(0.007,0.011)	(0.003,0.009)	9.33 ± 0.05	0.95	6.36 ± 0.04
04	(0.006,0.012)	(0.004,0.009)	9.07 ± 0.03	1	6.51 ± 0.02
04	(0.009,0.012)	(0.004,0.009)	9.11 ± 0.08	1	6.54 ± 0.06
04*	(0.007,0.012)	(0.0045,0.008)	10.2 ± 0.2	0.95	6.96 ± 0.15
05	(0.007,0.012)	(0.004,0.009)	9.34 ± 0.03	1	6.71 ± 0.02
05*	(0.007,0.012)	(0.004,0.009)	9.31 ± 0.04	0.95	6.35 ± 0.03
06	(0.006,0.012)	(0.004,0.009)	8.80 ± 0.03	1	6.32 ± 0.02
06*	(0.007,0.012)	(0.0045,0.0075)	10.6 ± 0.3	0.95	7.24 ± 0.23
07a	(0.007,0.011)	(0.003,0.009)	9.02 ± 0.07	1	6.47 ± 0.06
07b	(0.007,0.011)	(0.003,0.009)	9.48 ± 0.07	1	6.80 ± 0.06
08*	(0.007,0.011)	(0.004,0.009)	9.21 ± 0.06	0.95	6.28 ± 0.05
09a*	(0.007,0.013)	(0.0045,0.008)	9.62 ± 0.04	0.95	6.56 ± 0.03
09b*	(0.007,0.013)	(0.0045,0.008)	10.26 ± 0.07	0.95	7.00 ± 0.05
09c*	(0.007,0.013)	(0.0045,0.008)	10.55 ± 0.03	0.95	7.20 ± 0.02
10*	(0.007,0.012)	(0.004,0.008)	9.54 ± 0.15	0.95	6.50 ± 0.11
11*	(0.007,0.013)	(0.0045,0.008)	10.48 ± 0.45	0.95	7.15 ± 0.34
11*	(0.007,0.013)	(0.0065,0.008)	9.81 ± 0.40	0.95	6.69 ± 0.30

Table 1.1: Effective target thicknesses based on LHRS singles yields. The effective thickness is determined from the average yield using equation 7.1. A * indicates reversed raster currents. Radiative corrections have been applied to the subtracted carbon spectrum. Raster changed between kin07a and kin07b, see table 7.11. Raster changed during kin09a,b,c, see table 7.13.

kin	cutsx	cutsy	average yield $\times 10^7 / \text{Coulomb}$	normalization factor	effective thickness $\times 10^{20} / \text{cm}^2$
02	(0.006,0.013)	(0.006,0.0085)	13.92 ± 0.14	1	10.26 ± 0.11
03*	(0.0095,0.013)	(0.005,0.008)	14.57 ± 0.01	0.95	10.21 ± 0.01
04	(0.007,0.012)	(0.006,0.009)	13.62 ± 0.05	1	10.05 ± 0.04
04*	(0.009,0.013)	(0.005,0.008)	15.3 ± 0.2	0.95	10.75 ± 0.15
05*	(0.01,0.013)	(0.005,0.008)	14.77 ± 0.14	0.95	10.35 ± 0.1
06	(0.007,0.012)	(0.006,0.009)	13.12 ± 0.1	1	9.68 ± 0.08
07*	(0.01,0.013)	(0.005,0.008)	14.5 ± 0.4	0.95	10.18 ± 0.3

Table 1.2: Bismuth effective target thicknesses based on LHRS singles yields. The effective thickness is determined from the average yield using equation 7.1. A * indicates reversed raster currents. The bismuth effective thickness includes an additional factor of 82/83 to account for the extra proton in bismuth compared to lead and a factor of 1.04 to account for radiative differences.

Chapter 2

Initial Target Configurations

The targets as initially installed during run1(March, 2007) and run2(January, 2008) are shown in tables 2.1, 2.2 and 2.3.

foil no.	mass (g)	dimensions inches	mg/cm^2
1	0.3075	0.999x0.999	47.76
2	0.2962	0.998x0.996	46.19
3	0.2989	0.998x0.999	46.47
4	0.2541	0.999x0.999	39.46
5	0.2704	0.998x1.000	42.00
6	0.3366	0.998x1.001	52.23
7	0.3740	0.998x1.001	58.03
8	0.3542	0.998x1.000	55.01
9	0.3122	0.996x0.998	48.86
10	0.3336	0.996x1.000	51.92

Table 2.1: Run 1, March 2007, diamond foils as per Phil Adderley, email June 12, 2008.

ladder position	material 1	material 2	material 3
1	BeO, $149 mg/cm^2$		
2	C, $83.8 mg/cm^2$		
3	diamond 1 307.5 mg $47.76 mg/cm^2$	lead 4, ^{208}Pb 1134 mg $194.8 mg/cm^2$	diamond 2 296.2 mg $46.19 mg/cm^2$
4	diamond 3 298.9 mg $46.47 mg/cm^2$	lead 5, ^{208}Pb 1128 mg $193.7 mg/cm^2$	diamond 4 254.1 mg $39.46 mg/cm^2$
5	diamond 5 270.4 mg $42.00 mg/cm^2$	bismuth 1, ^{209}Bi 1320 mg $204.6 mg/cm^2$	diamond 6 336.6 mg $52.23 mg/cm^2$

Table 2.2: Run 1, March 2007, from Dave Meekins, February 27, 2007. Target ladder is tilted at 30 degrees.

target	material	diamond foils no. masses	diamond total <i>mg/cm²</i>
thick lead no tilt	²⁰⁸ Pb, 3314 mg 0.5 mm	11,12 263.7 mg, 292.9 mg	86.34
thick lead 30 deg tilt	²⁰⁸ Pb, 3284 mg 0.5 mm	14,16 275.0 mg, 274.2 mg	85.1
thin lead 30 deg tilt	²⁰⁸ Pb, 1120 mg 0.17 mm	1,2 316.0 mg, 225.0 mg	83.86
bismuth	²⁰⁹ Bi, 1302 mg 0.207 mm 46.47 <i>mg/cm²</i>	8, 10 354.9mg, 333.5 mg 193.7 <i>mg/cm²</i>	106.8 39.46 <i>mg/cm²</i>
Carbon 2mm holey			
¹² C	84.2 <i>mg/cm²</i>	per email from Meekins	
¹⁸¹ Ta	18 <i>mg/cm²</i>	Jan. 21, 2008	
BeO	149 <i>mg/cm²</i>		
empty			

Table 2.3: Run 2, January, 2008 from top to bottom. Targets are 1"x1", per Phil Adderley and Dave Meekins.

Chapter 3

Introduction

During E06007 in March, 2007 the left spectrometer was fixed in momentum and angle ($\theta_L = 21.44^\circ$). The first few runs, up to run 1214, were inadvertently run with the left spectrometer at $\theta_L = 22.4^\circ$. Target Pb4 was damaged due to high current running. Target Pb3 starting at run 1376 was ramped up from a few microamps to usually less than 44 microamps. This gave us the opportunity to follow the counting rate of the Pb3 target from a condition where the target thickness was known from the weight/size measurements to the higher currents where the target morphology may have changed. Since the left spectrometer can serve as a luminosity monitor we should be able to determine the actual amount of heavy metal in the beam through out the experiment. The diamond layers on the lead and bismuth targets were weighed and measured. We will assume that the diamond foils were uniform in thickness to enable us to subtract the carbon contribution to the singles spectra in the left arm. The excess counts are then attributable to heavy metal material. A complication of the experiment is that the target frame was sometimes in the beam. We need to apply raster cuts to be sure that the singles spectrum is not contaminated by target frame hits. A crucial ingredient in the cross section determination is the assurance that the raster distribution is uniform since this is the only way we can extract the relevant charge passing through the target compared to the total charge. Since the beam current monitors feed ungated scalers we can not require them to count only if the electron has passed through a particular portion of the raster pattern.

The first step in the analysis is to check the singles spectra in the left HRS for the graphite target. The normalized yield per microamp should be independent of the raster cut if the raster pattern is uniform. The raster electronics was faulty in the early part of the run and it failed at run 1624. New raster electronics were installed after run 1624 but the leads driving the currents or going into the ADCs were accidentally switched.

3.1 Counting rate and target/beam morphology

Imagine an electron incident on a target material of area $dA = dx dy$ and the cross section for a nucleus is $d\sigma = (d\sigma/d\Omega)\Delta\Omega$. Then the probability for a collision is $dP = d\sigma/dA$. If the target density is ρ and the target thickness is $z(x, y)$ then the probability for a collision with any of the nuclei is then $dP = d\sigma/dA(\rho dAz(x, y)) = d\sigma\rho z(x, y)$. Suppose the electron flux over the target is $\phi(x, y)$ then the number of electrons in time dt through the area dA is $dN_e = \phi(x, y)dAdt$. The rate of collisions, dN/dt , over a target material of macroscopic area A is then

$$dN/dt = \int_A dx dy \phi(x, y) \rho(x, y) z(x, y) \int_{\Omega} (d\sigma/d\Omega) d\Omega(x, y). \quad (3.1)$$

Using the approximation that we can determine the average cross section for small beam size by

$$\int_{\Omega} (d\sigma/d\Omega) d\Omega(x, y) = \langle d\sigma/d\Omega \rangle \Delta\Omega. \quad (3.2)$$

We rewrite equation 3.1 as

$$dN/dt = \langle d\sigma/d\Omega \rangle \Delta\Omega \int_A dx dy \phi(x, y) \rho(x, y) z(x, y). \quad (3.3)$$

In the case that the target has constant density and is of constant thickness z_0 , equation 3.3 becomes

$$dN/dt = \langle d\sigma/d\Omega \rangle \Delta\Omega \rho z_0 \int_A dx dy \phi(x, y). \quad (3.4)$$

Where equation 3.4 is usual for small beam sizes where the integral now just gives the total electron rate. In the case where the electron flux is uniform, $\phi_0 = (1/A_T)dN_e/dt$ and A_T is the total area of the rastered beam, we can take $\phi(x, y)$ out of the integral and equation 3.3 becomes

$$dN/dt = \langle d\sigma/d\Omega \rangle \Delta\Omega \phi_0 \int_A dx dy \rho(x, y) z(x, y). \quad (3.5)$$

Equation 3.5 is the one of interest in the case where we have a large raster pattern but the target morphology changes.

The strategy we will follow is to tabulate the singles LHRS yield for low beam currents where the heavy metal targets do not suffer damage. The assumption is that target density and thickness is constant. Using equation 3.5 we can determine the physics constant $\langle d\sigma/d\Omega \rangle \Delta\Omega$. Since this quantity will not change as the target deforms we compare the singles yields to the low current running to obtain the number of target nuclei in the beam for higher current running. Suppose we compare two runs. Run 0 is taken when the target thickness is known and with a rastered beam of area A_{T0} . Then integrating

over time the total number of electrons per unit area for run 0 is N_0/A_{T0} . The piece of the raster pattern we choose for run 0 has area A_0 . The total singles spectrum yield is S_0 . The physics constant is thus:

$$\langle d\sigma/d\Omega \rangle \Delta\Omega = S_0/((N_0/A_{T0})A_0z_0\rho). \quad (3.6)$$

For any subsequent run, say run 1 where the number of incident electrons is N_1 , the total raster pattern area is A_{T1} , the piece of the raster pattern we use to generate the singles spectrum is A_1 and the singles yield is S_1 then using equation 3.6 we have:

$$S_0/((N_0/A_{T0})A_0z_0\rho) = S_1/((N_1/A_{T1}) \int_{A_1} dx dy \rho(x, y) z(x, y)). \quad (3.7)$$

The integral in equation 3.7 is the total number of target nuclei in the selected area A_1 .

$$\int_{A_1} dx dy \rho(x, y) z(x, y) = (S_1/S_0)(N_0/N_1)(A_{T1}/A_{T0})(A_0z_0\rho). \quad (3.8)$$

We can also recast the equations to get an effective density in terms of *nuclei/cm²*. Since

$$S_1 = \langle d\sigma/d\Omega \rangle \Delta\Omega (N_1/A_{T1}) \int_{A_1} dx dy \rho(x, y) z(x, y). \quad (3.9)$$

then we can rewrite the integral over density as $\int_{A_1} dx dy \rho(x, y) z(x, y) = \bar{\rho} \bar{z}$ so

$$S_1 = \langle d\sigma/d\Omega \rangle \Delta\Omega N_1 (A_1/A_{T1}) \bar{\rho} \bar{z}. \quad (3.10)$$

and $N_1(A_1/A_{T1}) = Q_{effective1}$ which is the fraction of electrons contributing to the counts S_1 , so

$$S_1 = \langle d\sigma/d\Omega \rangle \Delta\Omega Q_{effective1} \bar{\rho} \bar{z}. \quad (3.11)$$

The factor $\bar{\rho} \bar{z} = \rho_{eff}$ is the effective density *nuclei/cm²*. We write for the case where we know the real target density and thickness

$$S_0 = \langle d\sigma/d\Omega \rangle \Delta\Omega Q_{effective0} \rho_0 z_0. \quad (3.12)$$

From these relations we can equate the ratios

$$\frac{S_1/Q_{effective1}}{S_0/Q_{effective0}} = \frac{\bar{\rho} \bar{z}}{\rho_0 z_0}. \quad (3.13)$$

Chapter 4

Graphite data

The graphite target serves two purposes. It will allow us to test various combinations of selected raster areas and compare to the unrastered beam. This gives us a measure of the reliability of the singles luminosity technique. The graphite target is also needed to subtract the effects of the diamond foils. Cuts used in the graphite analysis are shown here.

```
TCut deltaL = "abs(L.gold.dp)<0.050";
TCut deltaR = "abs(R.gold.dp)<0.045" ;
TCut anglesL="(L.gold.ph>-0.030&&L.gold.ph<0.030)&&(L.gold.th>-0.060&&L.gold.th<0.080)";
TCut anglesR="(R.gold.ph>-0.060&&R.gold.ph<0.060)&&(R.gold.th>-0.170&&R.gold.th<0.170)";
TCut Lgoldp = "(L.gold.p<2.2 && L.gold.p>1.8)";
TCut YtargL = "abs(L.gold.y)<0.01";
TCut Goodpath1 = "((L.tr.path1>24.5)&&(L.tr.path1<26))";
TCut trig1 = "(D.evtypebits&0x02)==0x02";
TCut trig2 = "(D.evtypebits&0x04)==0x04";
TCut trig3 = "(D.evtypebits&0x08)==0x08";
TCut trig4 = "(D.evtypebits&0x10)==0x10";
TCut trig5 = "(D.evtypebits&0x20)==0x20";
TCut trig6 = "(D.evtypebits&0x40)==0x40";
TCut trig7 = "(D.evtypebits&0x80)==0x80";
// raster cuts change with kinematics
TCut rastx = "(ReactPt_L.x>0.006)&&(ReactPt_L.x<0.012)";
TCut rasty = "(ReactPt_L.y>0.004)&&(ReactPt_L.y<0.009)";
//
TCut GoodLeft3 = trig3&&Goodpath1&&YtargL&&anglesL&&deltaL&&rastx&&rasty;
TCut GoodLeft5 = trig5&&Goodpath1&&YtargL&&anglesL&&deltaL&&rastx&&rasty;
```

An example of a raster pattern for kin04 is shown in figure 4.1. The singles and coincidence momentum spectra for kin04 are shown in figure 4.2. A spreadsheet is stored on the ELOG page which tabulates the LHRS normalized momentum spectra. The definitions of the terms in the spreadsheet are in table 4.1. Note that wire chamber efficiencies have not been included. The

name of correction or parameter	correction or parameter
target	Pb or C-on/off, lead or carbon raster on/off
I(uA)	current in microamps
ps3	prescale factor for trigger 2
Q(C)	total charge in Coulombs using Joaquin's BCM coefficients
t3	trigger 3 counts allowed through by DAQ
t3_scaler	trigger 3 scaler counts
Live time	DAQ Live time = ps3*t3/t3_scaler
L.gold.dp	singles momentum spectrum for LHRS surviving cuts
L.gold.dp, t5	LHRS momentum spectrum for trigger 5
edtpl	LHRS scaler electronic dead time pulser counts going through coincidence electronics
edtmnt	electronic dead time monitor pulser scaler
edt live	electronic dead time edtpl/edtmnt
frac raster	A_1/A_{1T} , fraction of area cut to total raster pattern
L.gold.dp/Q*ps3/(frac raster)	$ps3*L.gold.dp/(Live\ time)/(frac\ rast)/Q + (L.gold.dp,t5)/(edt\ live)/(frac\ rast)/Q$

Table 4.1: Quantities in the spreadsheet used to determine number of nuclei in the beam.

electronic dead time, edt live, is larger than the DAQ dead time, Live time, by a seemingly too big a difference. Both the trig3 and trig5 spectra are included with the proper normalization to yield the LHRS momentum spectra. A study of the stability of the luminosity technique for the graphite target is in table 4.2. This table includes only runs before the raster failure.

Table 4.3 shows the normalized singles rates for runs after 1624 but uses the same raster "correction" as table 4.2, even though the raster leads were switched.

Once the correct raster correction for the momentum spectra is applied after run 1624 the table can be completed for the full run. In general the unrastered beam gives a larger rate than the rastered beam. There is about a 7% difference for kin01-kin11 and a 2.5% difference for kin13. Ideally the rastered beam would give the same normalized yield independent of the raster size for a uniform raster and uniform target.

kin	run number	target	current μ A	raster fraction	LHRS singles, normalized $\times 10^7$
kin01	1230	C-on	45.9	0.406	4.881
	1518	C-on	36	0.416	4.844
	1519	C-on	36	0.416	4.871
	1520	C-off	32	NA	5.191
kin02	1231	C-on	46.4	0.406	4.874
	1232	C-off	47.7	NA	5.244
kin04	1339	C-on	39	0.513	4.925
	1345	C-on	56	0.513	4.983
kin06	1419	C-on	32.3	0.552	4.593
	1419	C-on	32.3	0.368	4.548
	1420	C-on	37	0.552	4.565
kin07	1541	C-off	33	NA	5.147
	1556	C-on	23	0.410	4.937
kin05	1610	C-on	36	0.476	5.052
*kin13	1490	C-on	24	0.325	0.0676
	1491	C-on	38	0.325	0.0697
	1492	C-on	40	0.325	0.0722
	1493	C-on	39	0.325	0.0696
	1502	C-on	38	NA	0.0717
*kin12	1506	C-on	39	0.325	0.3751

Table 4.2: Normalized LHRS singles counts for rastered and unrastered beam for the graphite target. Raster leads in the correct configuration. Average singles rastered yield for $\theta_L = 21.44^\circ$ is $4.83 \pm 0.17 \times 10^7$. *For kin12 and kin13 the LHRS was moved to new angles and central momenta.

kin	run number	target	current μ A	raster fraction	LHRS singles, normalized $\times 10^7$
kin02	1731	C-on	35.5	0.381	5.133
	1732	C-on	37.6	0.381	5.085
	1733	C-on	38.7	0.381	5.084
kin03	1645	C-on	31	0.381	5.082
	1646	C-on	36.8	0.381	5.050
	1647	C-on	36.8	0.381	5.058
kin08	1690	C-on	27	0.381	5.026
	1692	C-on	21	0.381	5.097
	1696	C-on	17	0.381	5.023
kin10	1773	C-on	14	0.410	5.161
	1777	C-on	13	0.410	5.161
	1782	C-on	28	0.410	5.296

Table 4.3: Normalized LHRS singles counts for rastered beam for the graphite target. Raster leads are in the inverted configuration but raster correction for normal lead configuration was used. Average singles yield = $5.11 \pm 0.08 \times 10^7$.

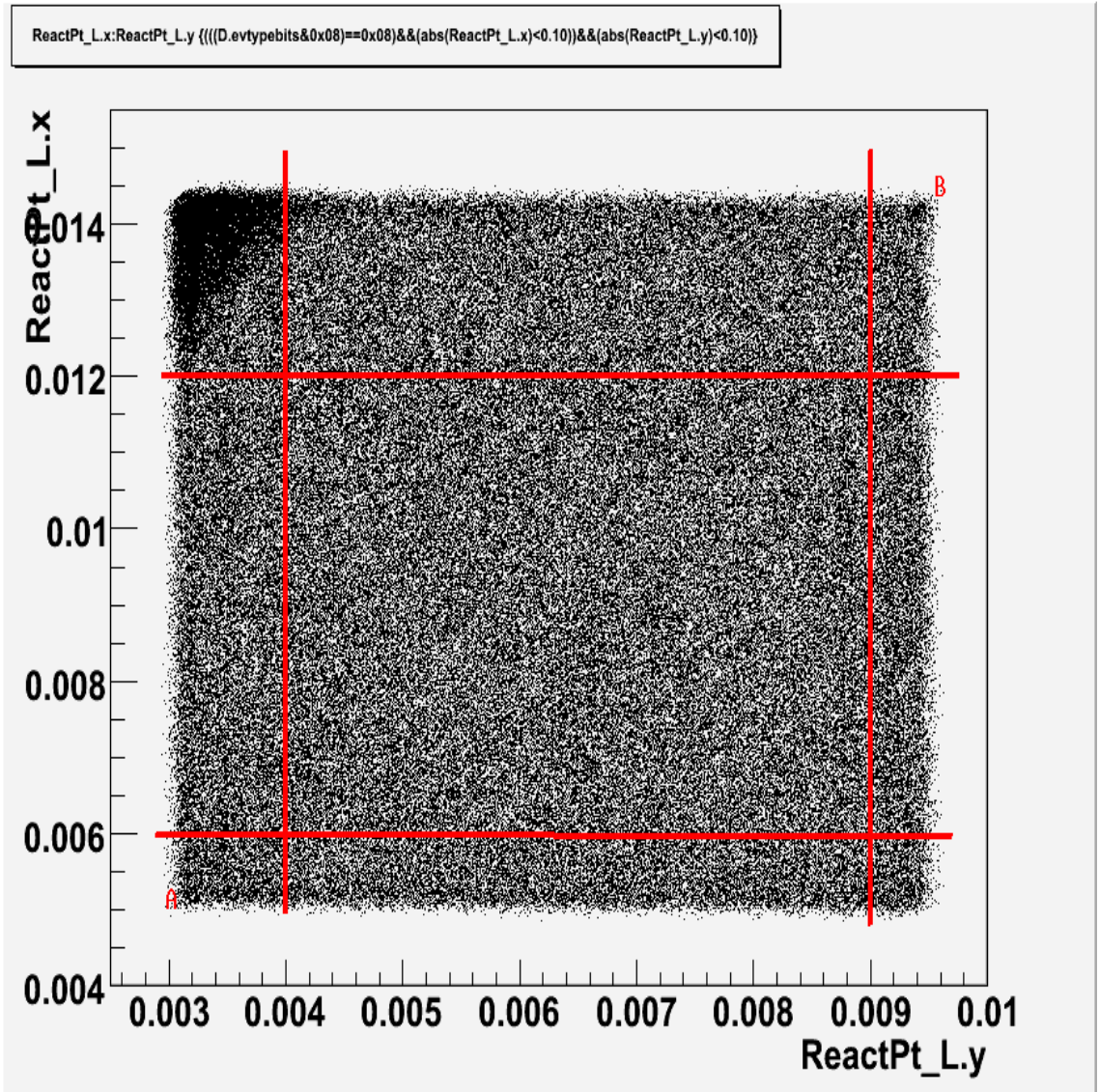


Figure 4.1: Sample of a raster pattern with typical cuts shown. Points A and B at the corners determine the total area of the raster, A_T . The rectangle shows the area A used in the LHRS cut to generate the singles spectrum.

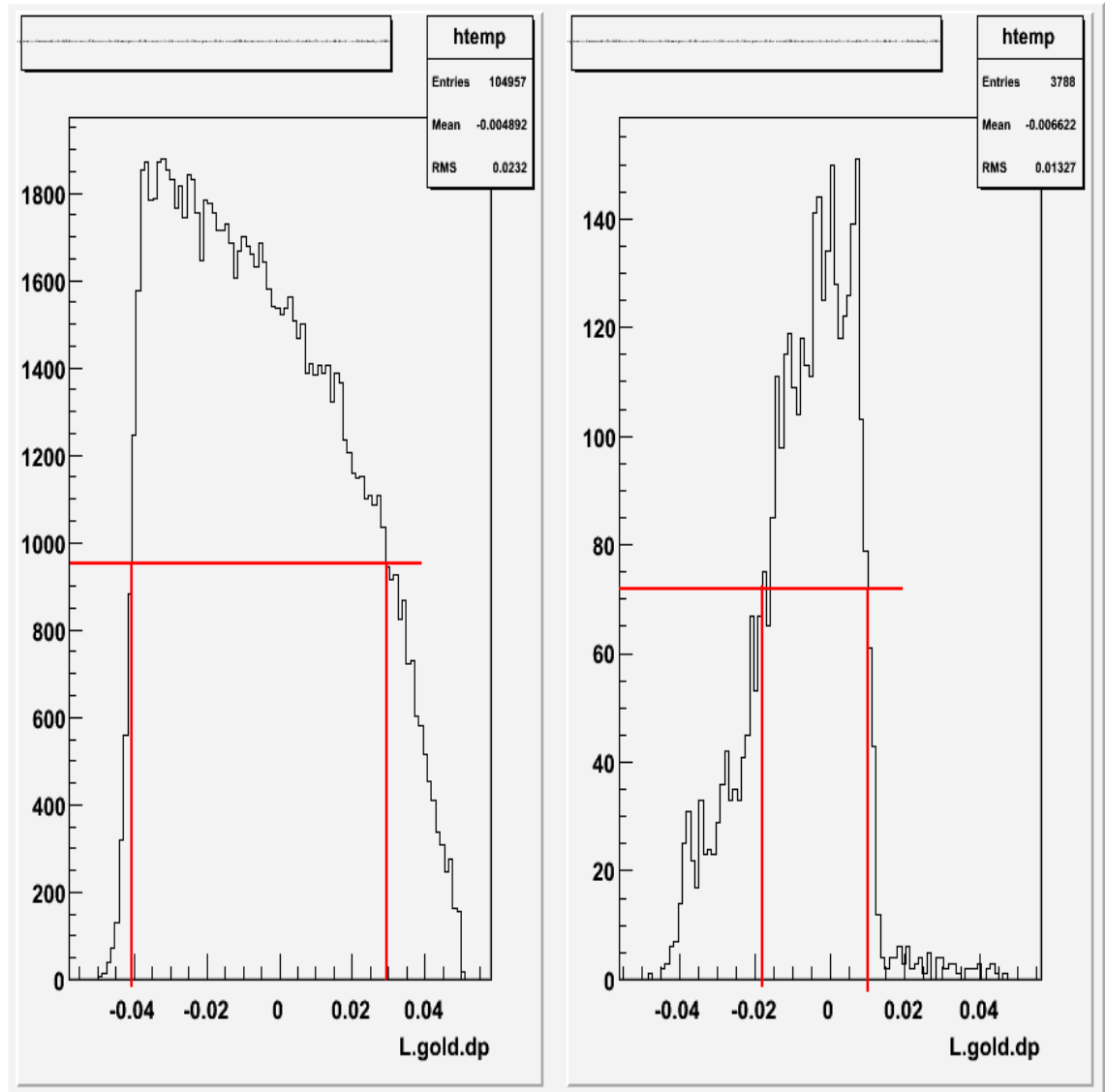


Figure 4.2: Sample of a singles and coincidence momentum spectra in the LHRS with typical cuts.

Chapter 5

Graphite results

A comparison of the yields in table 4.2 shows that for the rastered beam the normalized yield is $\text{yield1} = 4.83 \pm 0.17 \times 10^7$ which is a 4% standard deviation in the assumed target thickness by the luminosity comparison. The few yields for the unrastered beam give an average of $5.19 \pm 0.05 \times 10^7$, or a 1% spread in the assumed target thickness. Since we must use the rastered beam and cut on the raster pattern to avoid the frame the luminosity procedure limits our knowledge of the heavy metal target thickness to no better than $\pm 4\%$.

In the case of the inverted raster leads but applying the normal raster correction, see table 4.3 the average singles yield with the raster on is $\text{yield2} = 5.11 \pm 0.08 \times 10^7$. The ratio $\text{yield1}/\text{yield2}$ is 0.95 ± 0.04 . This factor can be applied to the heavy metal target thickness results after run 1624.

A study of the counting rate as a function of raster cut on the graphite target was made for runs 1518+1519. The plot showing the matrix of cuts is in figure 5.1. The summed counts from runs 1518+1519 for these areas is

Raster pattern graphite counts for kin01, runs 1518+1519 for trigger 3

raster x	raster y				
(0.010,0.011)	12253	12373	12173	11921	11689
(0.009,0.010)	12495	12505	11947	12111	11773
(0.008,0.009)	12270	12211	11748	11991	11830
(0.007,0.008)	12507	12240	12102	12305	12046
	(0.004,0.005)	(0.005,0.006)	(0.006,0.007)	(0.007,0.008)	(0.008,0.009)

average = 12125, std.dev. = 254, sqrt(12125) = 110

There is a standard deviation of a factor of 2.5 bigger than what is expected

from statistics alone. From this result we can not determine if these fluctuations in counts are due to non uniformity of the graphite target or to beam modulation effects.

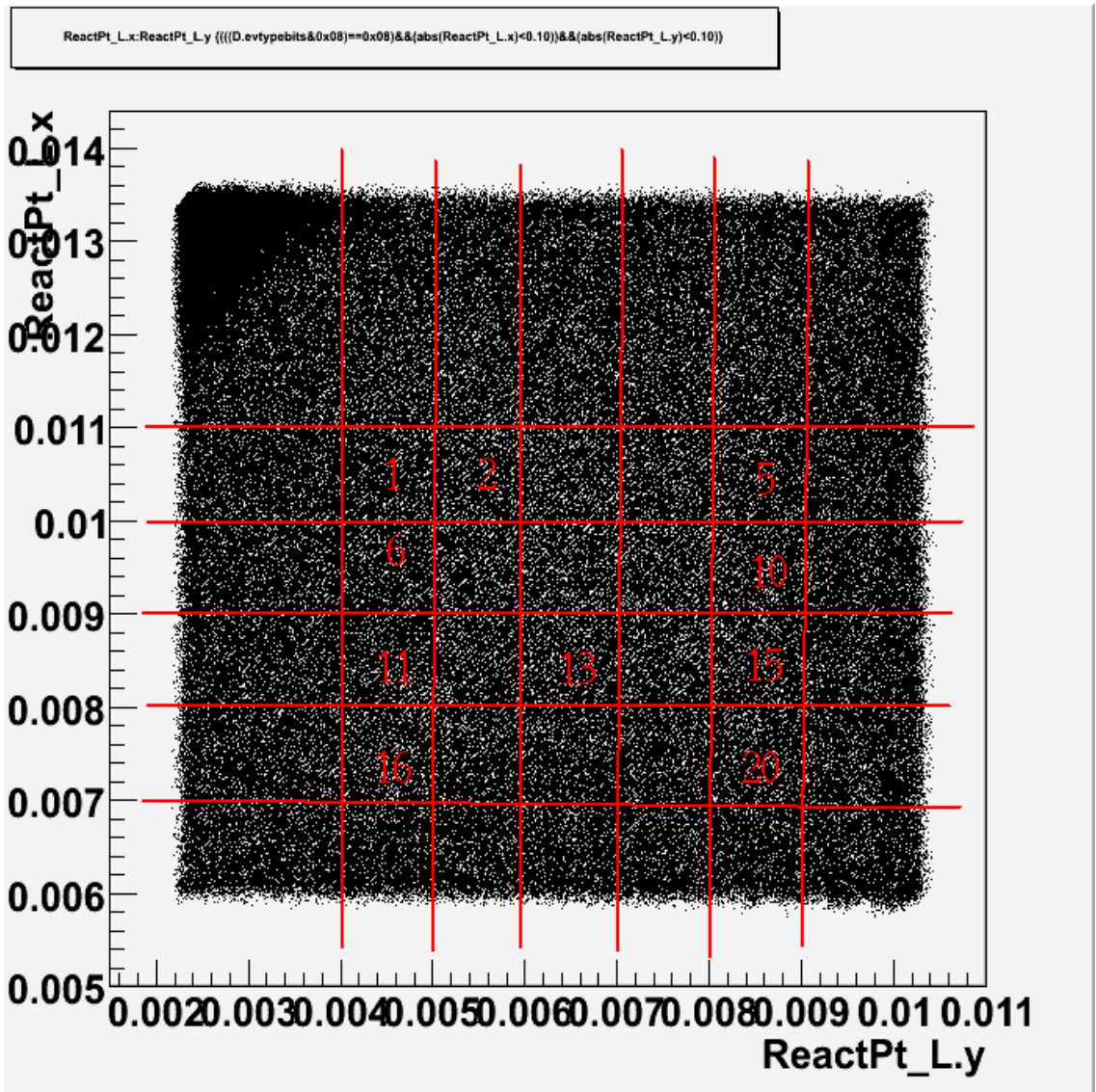


Figure 5.1: Reaction point for run 1518. The matrix shows the areas of the raster patterned investigated to determine uniformity in count rate. Counts in the 20 small regions were tallied.

Chapter 6

GEANT simulations of carbon spectrum in lead

The graphite singles spectrum can be used to deduce the corresponding carbon singles spectrum from the lead/diamond sandwich. The correspondence will be a first approximation since the diamond foils straddle the lead foil. It would not be possible to do the simulation with this exact geometry because we do not have a spectrum from carbon after the electron beam has passed through the lead. However, electrons from the upstream and downstream foils must all have passed through the lead, either after scattering in the upstream foil or from the downstream foil after the beam has passed through the lead. The simulation described here compares the measured graphite spectrum to that spectrum after it has passed through the lead foil. Since the other sources of radiation, such as the kapton windows, titanium windows and air, are already included in the graphite spectrum, for the lead simulation all windows are removed so only the effect of the lead is included. Figure 6.1 shows the measured graphite spectrum (solid curve) and the spectrum after passing through 0.17mm of lead tilted at 31deg. The spectrometer acceptance cuts off the dp spectrum below -0.03 so the comparison between graphite and graphite+lead can be made for $-0.03 \leq dp \leq +0.05$. The ratio of areas for this interval is 0.82, which implies that the carbon contribution from the diamond foils is reduced by a factor of 0.82 compared to the counts from pure graphite.

A plot of actual data, the LHRS singles spectra from pb3 and graphite is shown in figure 6.2. The solid curve is from pb3 and the dashed from the graphite target. The spectra are normalized at $dp = -0.03$. From this figure it appears that the spectra match each other in shape very well. However, as seen in the simulation, figure 6.1, there should be a difference in shape with the lead spectrum underestimating the graphite spectrum for dp greater than -0.03. Since we do not have the spectrum for either graphite or lead above $dp=0.05$ we don't know how much more there might be for lead than carbon. The fact that the data for pb3 and graphite fit well may be a result of a greater yield

	kin1-11	kin12	kin13
$p_0(GeV/c)$	2.216	1.902	1.602
$\theta_L(deg)$	21.44	30.59	39.72
rad. loss factor	0.82	0.76	0.66

Table 6.1: Momenta and angles for the LHRS. The rad. loss factor is to be multiplied against the normalized graphite yield to account for radiative losses of events from the diamond foils due to the heavy metal foil.

above $dp=0.05$ for lead which gets fed down by radiation to fill in the lack of events predicted by the geant simulation.

Geant simulations were also performed for kinematics 12 and 13. Although the LHRS was moved for these two measurements it is still of interest to compare the carbon yields to that of the lead target(pb3). Figures 6.3 and 6.4 show the measured graphite spectra and the effects of the lead target on these spectra.

There are significant radiative losses for these LHRS angles as shown in table 6.1. These radiative losses must be included to properly subtract the contribution of the diamond foils to the total rate seen from the heavy metal targets.

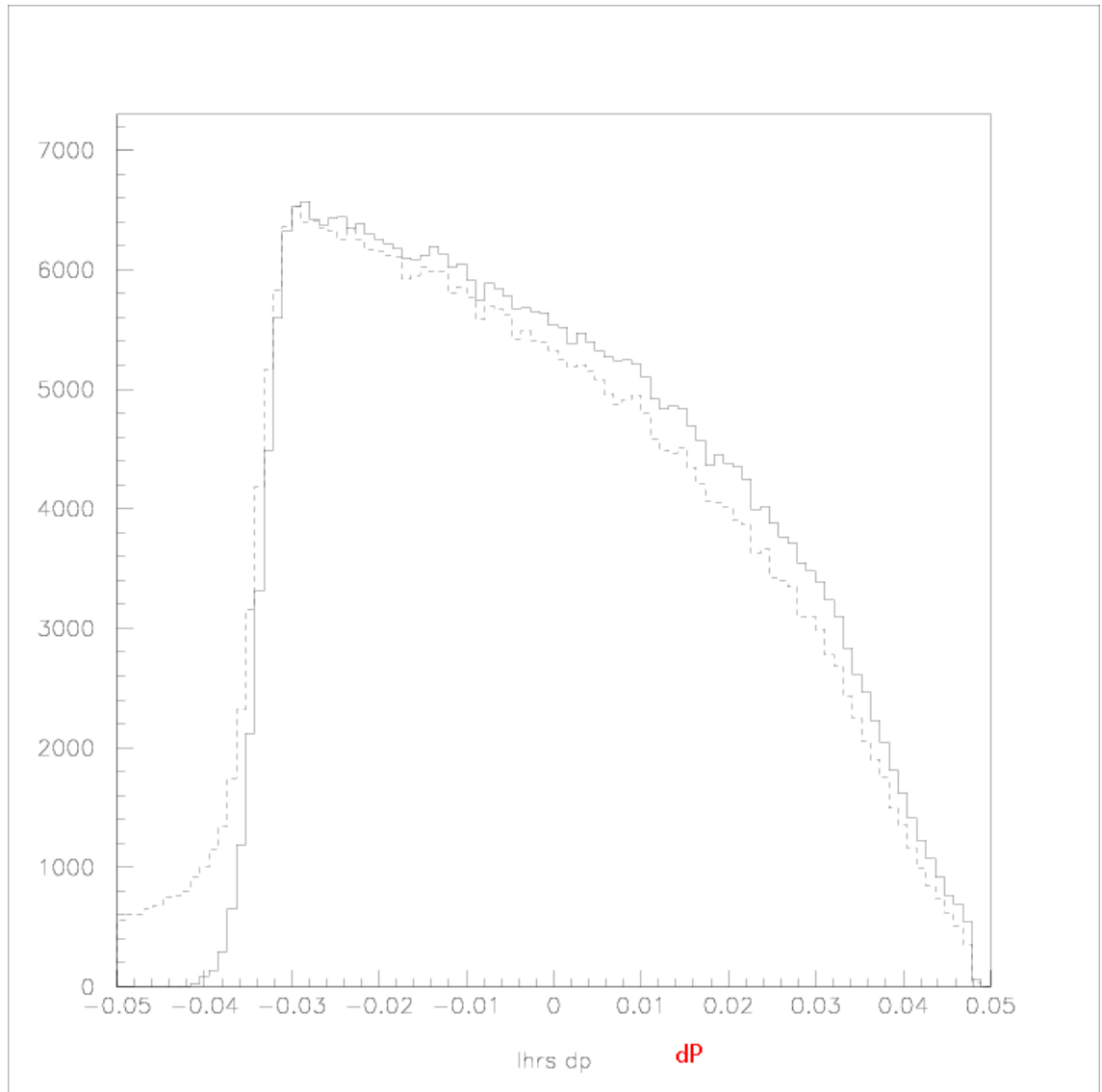


Figure 6.1: The solid curve is the measured graphite spectrum. The dashed curve shows the geant predicted spectrum. The two curves are normalized to each other at $dp = -0.03$ and were generated for the same number of electrons in the input file(the measured graphite spectrum).

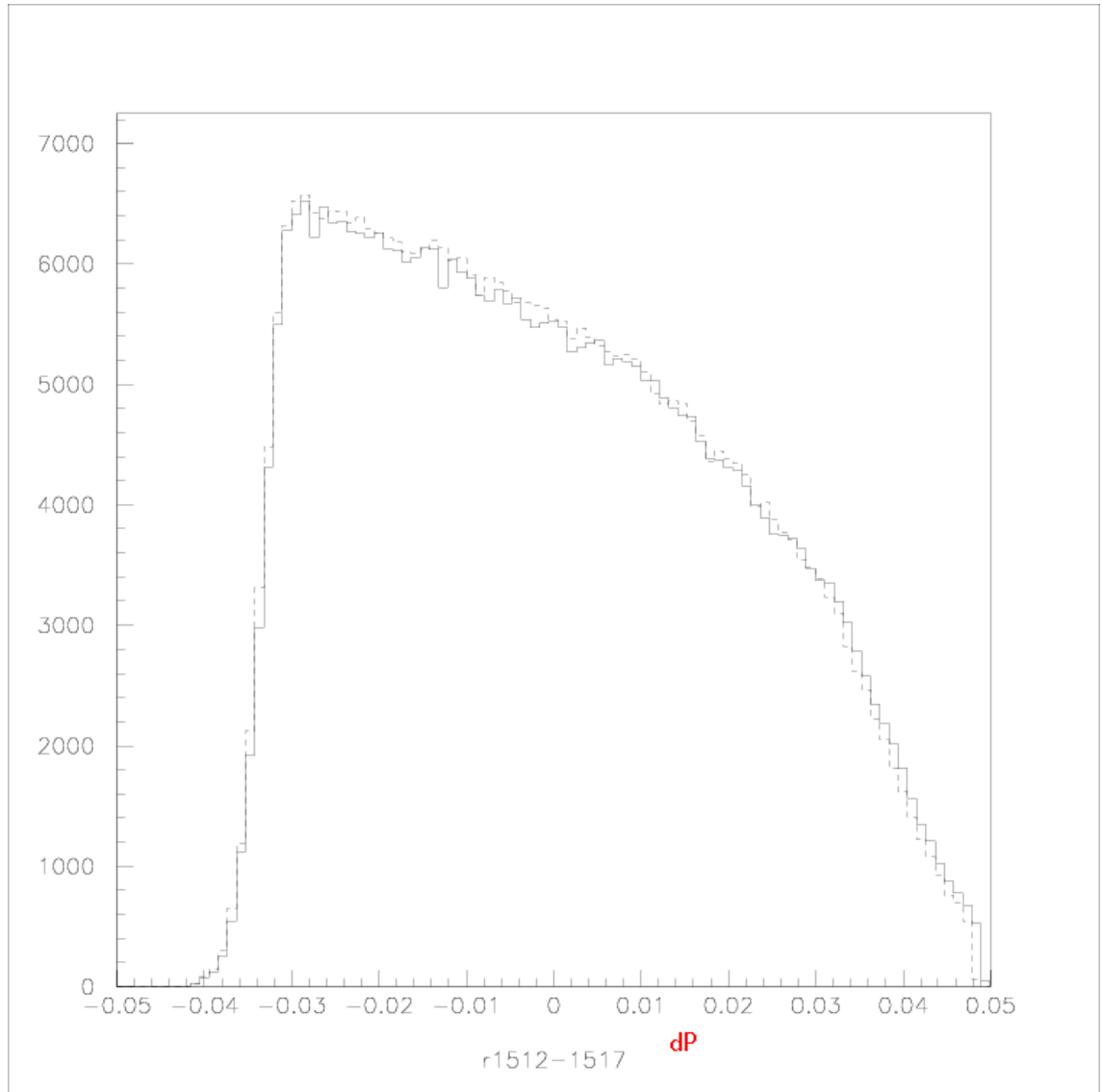


Figure 6.2: The solid curve is the measured lead(pb3) spectrum. The dashed curve shows the measured graphite spectrum. The two curves are normalized to each other at $dp = -0.03$.

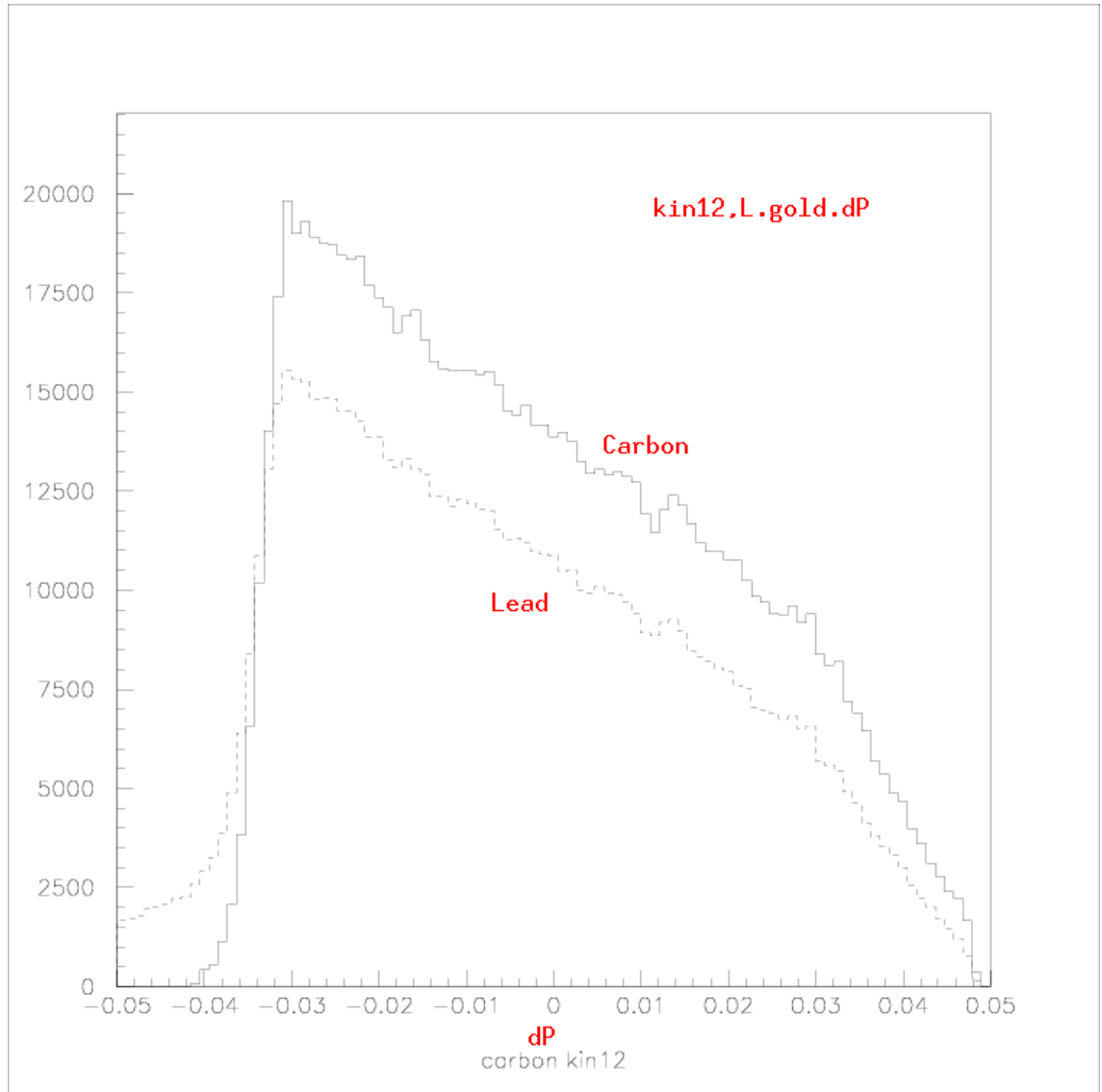


Figure 6.3: The solid curve is the measured graphite spectrum for kinematics 12. The dashed curve shows the geant predicted spectrum after passing through the lead target.

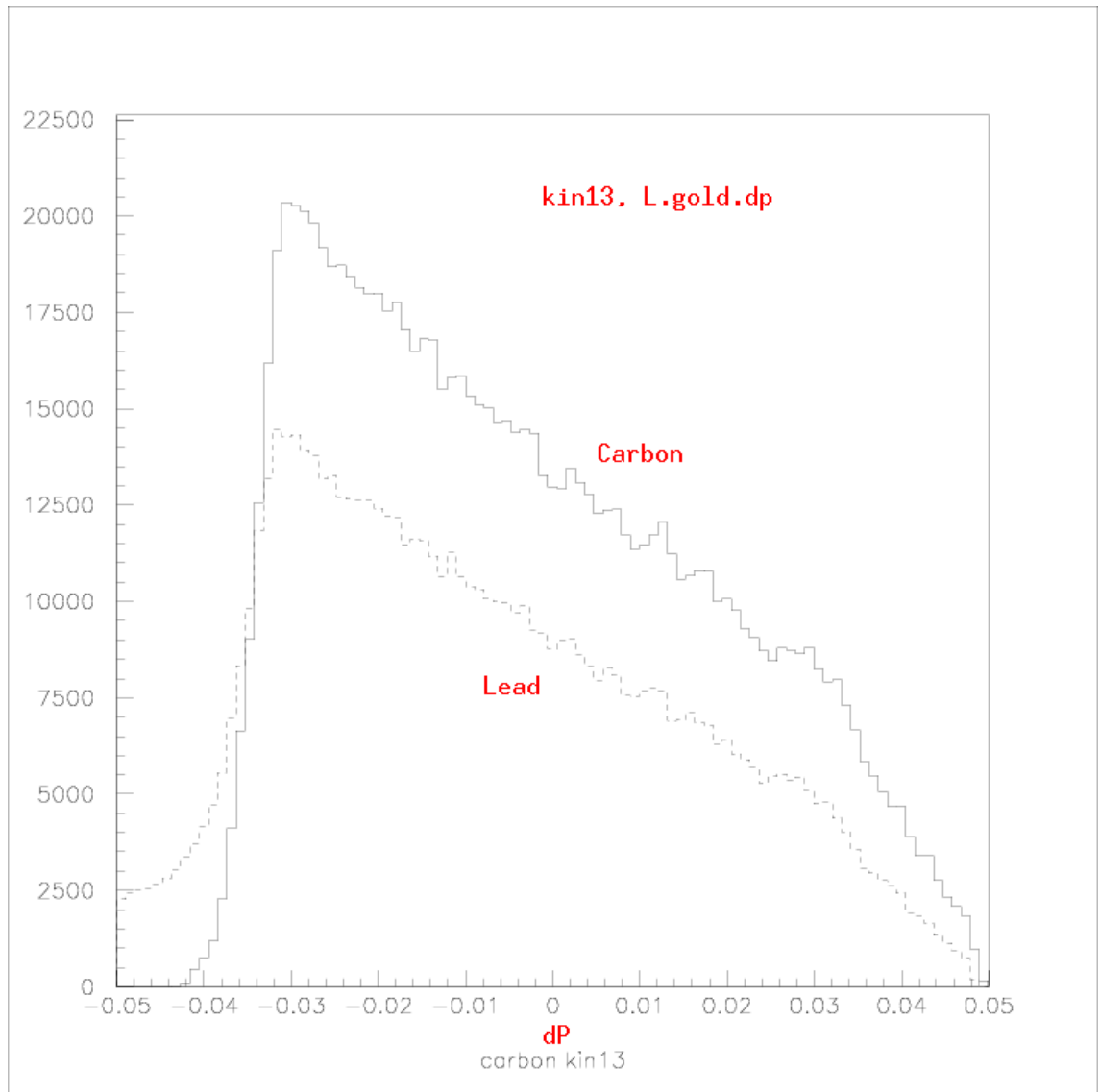


Figure 6.4: The solid curve is the measured graphite spectrum for kinematics 13. The dashed curve shows the geant predicted spectrum after passing through the lead target.

Chapter 7

Lead data

7.1 Lead data

The normalized count rate changes for some of the lead target 3(pb3) runs. A visual example is seen in figures 7.3 and 7.5. The bluer shades in the lower right corner of figure 7.3 shows a thinner target than the more uniform distribution seen in figure 7.5. The raster size was reduced between these runs and there is about a 5% difference in normalized yield. An adjustment of the effective charge had to be made since we are assuming the charge is proportional to the area of the cut. A run by run comparison of the normalized counting rates can be expected to change if the heavy metal flows about the diamond substrate under the electron beam. However, even if a change in target thickness occurs on a point by point basis, the total number of nuclei in the beam may stay the same.

run number normal raster currents	current μ A	carbon+lead singles $\times 10^7$	lead singles $\times 10^7$
1512	37	12.86	8.854
1513	37	12.88	8.874
1514	36	12.88	8.881
1515	38	12.89	8.889
1516	35	12.89	8.889
1517	40	12.84	8.839

Table 7.1: kin01-Normalized LHRS singles counts for the pb3 target. Normal raster currents. raster pattern r1518, A(.006,.0023),B(.0134,.0101), cutsx(.007,.011),cutsy(.003,.009)

run number reversed raster currents	current μ A	carbon+lead singles $\times 10^7$	lead singles $\times 10^7$
1721	10	13.29	9.287
1722	14	13.13	9.133
1723	40	13.19	9.192
1724	39	13.17	9.174
1725	24	13.18	9.183
1726	40	13.22	9.217

Table 7.2: kin01-Normalized LHRS singles counts for the pb3 target. Reversed raster currents. raster pattern r1723, A(.0061,.0028),B(.0134,.0098), cutsx(.007,.011),cutsy(.003,.009)

run number reversed raster currents	current μ A	carbon+lead singles $\times 10^7$	lead singles $\times 10^7$
1736	27	13.45	9.279
1737	39	13.47	9.298
1738	34	13.45	9.272
1769	37	13.46	9.281
1770	39	13.44	9.267
1771	39	13.43	9.256

Table 7.3: kin02-Normalized LHRS singles counts for the pb3 target. raster pattern r1731, A(.0060,0.0028),B(.0135,.0098),cutsx (.007,.011),cutsy(0.004,.009). Reversed raster currents.

run number reversed raster currents	current μ A	carbon+lead singles $\times 10^7$	lead singles $\times 10^7$
1648	9	13.56	9.365
1649	20	13.51	9.322
1650	40	13.51	9.316
1683	37	13.47	9.281
1684	35	13.53	9.339
1685	37	13.54	9.353

Table 7.4: kin03-Normalized LHRS singles counts for the pb3 target. raster pattern r1645, A(.006,.0028),B(.0135,.0098), cutsx(.007,.011),cutsy(.003,.009)

run number normal raster currents	current μ A	carbon+lead singles $\times 10^7$	lead singles $\times 10^7$
1376	0.9	13.93	9.863
1377	2	13.62	9.550
1378	4.3	13.18	9.117
1379	9.5	13.12	9.050
1380	9.7	13.16	9.095
1381	23.2	13.07	9.009
1382	24	13.16	9.096
1383	39	13.14	9.073
1418	38	13.29	9.095

Table 7.5: kin04-Normalized LHRS singles counts for the pb3 target. Normal raster currents. raster pattern r1339, A(.005,.003),B(.014,.0095), cutsx(.007,.012),cutsy(.004,.009), raster fraction = 0.513.

run number normal raster currents	current μ A	carbon+lead singles $\times 10^7$	lead singles $\times 10^7$
1376	0.9	13.97	9.911
1377	2	13.73	9.667
1378	4.3	13.30	9.237
1379	9.5	13.19	9.120
1380	9.7	13.25	9.187
1381	23.2	13.06	8.993
1382	24	13.24	9.175
1383	39	13.15	9.084
1418	38	13.18	9.111

Table 7.6: kin04-Normalized LHRS singles counts for the pb3 target. Normal raster currents. raster pattern r1339, A(.005,.003),B(.014,.0095), cutsx(.007,.012),cutsy(.004,.009), raster fraction = 0.256.

run number reversed raster currents	current μ A	carbon+lead singles $\times 10^7$	lead singles $\times 10^7$
1934	38	14.50	10.31
1935	38	14.47	10.29
1936	38	14.57	10.38
1950	34	14.49	10.30
1951	26	14.42	10.23
1952	18	13.95	9.758

Table 7.7: kin04-Normalized LHRS singles counts for the pb3 target. reversed raster currents. raster pattern r1339, A(.005,.003),B(.014,.0095), cutsx(.007,.012),cutsy(.004,.009)

run number mixed raster currents	current μ A	carbon+lead singles $\times 10^7$	lead singles $\times 10^7$
1611	9	13.52	9.367
1612	19	13.45	9.296
1613	37	13.50	9.346
1614	40	13.48	9.326
1621	40	13.53	9.382
1627*	39	13.41	9.292
1628*	38	13.47	9.316
1630*	40	13.46	9.310

Table 7.8: kin05-Normalized LHRS singles counts for the pb3 target. Mixed raster currents. raster pattern r1610, A(.006,.0028),B(.0135,.0098), cutsx(.007,.012),cutsy(.004,.009). run no.* means reversed raster currents.

run number normal raster currents	current μ A	carbon+lead singles $\times 10^7$	lead singles $\times 10^7$
1434	19.6	12.71	8.754
1435	39	12.75	8.786
1436	40	12.74	8.778
1437	38	12.79	8.834
1438	28	12.79	8.825
1439	35.6	12.78	8.816
1440	40	12.76	8.802
1485	40	12.79	8.831

Table 7.9: kin06-Normalized LHRS singles counts for the pb3 target. raster pattern r1419, A(.006,.0023),B(.01345,.01), cutsx(.007,.011),cutsy(.004,.009).

run number reverse raster currents	current μ A	carbon+lead singles $\times 10^7$	lead singles $\times 10^7$
1917	33	14.69	10.50
1918	36	14.80	10.61
1919	8	15.35	11.16
1928	36	14.66	10.47
1929	36	14.67	10.48
1930	33	14.70	10.52

Table 7.10: kin06-Normalized LHRS singles counts for the pb3 target. reversed raster currents. raster pattern r1917, A(.0054,.0037),B(.0140,.0089), cutsx(.007,.012),cutsy(.0045,.0075).

run number raster pattern changed during runs	current μ A	carbon+lead singles $\times 10^7$	lead singles $\times 10^7$
1521	9.5	12.94	8.906
1522	19.3	13.02	8.987
1523	36	12.99	8.965
1538	34	13.08	9.041
1551	36	13.09	9.057
1585	37	13.06	9.025
1593	36	13.06	9.134
1596*	29	13.53	9.499
1600*	35	13.65	9.613
1604*	37	13.46	9.428
1607*	36	13.47	9.433
1609*	36	13.44	9.402

Table 7.11: kin07-Normalized LHRS singles counts for the pb3 target. raster pattern r1541, A(.006,.0022),B(.0135,.01), cutsx(.007,.011),cutsy(.003,.009). *changed raster pattern r1596 A(x,y)=(0.0060,0.0028),B(0.0135,0.0098), cutsx(.007,.011),cutsy(.003,.009).

run number reversed raster currents	current μ A	carbon+lead singles $\times 10^7$	lead singles $\times 10^7$
1697	11	13.46	9.312
1698	19	13.40	9.250
1699	24	13.36	9.210
1714	37	13.32	9.167
1715	31	13.32	9.173
1716	17	13.28	9.128

Table 7.12: kin08-Normalized LHRS singles counts for the pb3 target. Reversed raster currents. raster pattern r1689, A(0.006,0.0028),B(.0135,0.0098), cutsx(0.007,0.011),cutsy(0.004,0.009)

run number reversed raster currents	current μ A	carbon+lead singles $\times 10^7$	lead singles $\times 10^7$
1859	38	13.83	9.566
1860	37	13.91	9.634
1861	38	13.92	9.647
1872*	37	14.58	10.31
1873*	37	14.46	10.19
1874*	37	14.57	10.30
1889**	37	14.84	10.57
1890**	34	14.79	10.51
1891**	37	14.82	10.55

Table 7.13: kin09-Normalized LHRs singles counts for the pb3 target. Reversed raster currents.
r1859, A(0.0054,0.0035), B(0.0139,0.0091), cutsx(0.007,0.013), cutsy(0.0045,0.008):
*r1873, A(0.0055,0.0037), B(0.0139,0.0088), cutsx(0.007,0.013), cutsy(0.0045,0.008):
**r1889, A(0.0062,0.0034), B(0.0132,0.009), cutsx(0.007,0.013), cutsy(0.0045,0.008)

run number reversed raster currents	current μ A	carbon+lead singles $\times 10^7$	lead singles $\times 10^7$
1798	38	13.75	9.480
1799	36	13.73	9.462
1800	37	13.75	9.482
1818	29	13.82	9.543
1819	21	14.17	9.902
1820	36	13.87	9.597
1826	25	13.75	9.480
1827	28	13.71	9.436
1828	23	13.70	9.430

Table 7.14: kin10-Normalized LHRS singles counts for the pb3 target. Reversed raster currents. raster pattern r1773,A(0.006,0.003), B(0.0135,0.0095), cutsx(0.007,0.012),cutsy(0.004,0.008).

run number reversed raster currents	current μ A	carbon+lead singles $\times 10^7$	lead singles $\times 10^7$
1895	18	14.41	10.14
1896	37	14.73	10.46
1897	34	14.76	10.48
1907	37	14.61	10.34
1908	27	14.66	10.39
1909	35	14.77	10.49
1913	24	14.88	10.61
1914	25	15.24	10.96
1915	25	14.69	10.42

Table 7.15: kin11-Normalized LHRS singles counts for the pb3 target. Reversed raster currents. raster pattern. r1895, A(0.0055,0.0037),B(0.0139,0.0088),cutsx(0.007,0.013),cutsy(0.0045,0.008), raster fraction = 0.490.

7.2 Lead target pb4

This was the first lead target to see the beam and we discovered it was damaged early on in the first run of kin01, figure 7.1. This growing hole was not discovered during the online replay but established in the offline analysis during the run. By kin02 the hole was substantially larger, figure 7.2. Nevertheless, lead was still present in the beam so in tables 7.17 and 7.18 the run by run singles yields are presented.

run number reversed raster currents	current μ A	carbon+lead singles $\times 10^7$	lead singles $\times 10^7$
1895	18	13.83	9.560
1896	37	14.08	9.805
1897	34	14.13	9.858
1907	37	13.93	9.658
1908	27	13.94	9.670
1909	35	14.11	9.842
1913	24	14.20	9.926
1914	25	14.51	10.24
1915	25	14.02	9.744

Table 7.16: kin11-Normalized LHRS singles counts for the pb3 target. Reversed raster currents. raster pattern. r1895, A(0.0055,0.0037),B(0.0139,0.0088),cutsx(0.007,0.013),cutsy(0.0045,0.0065),raster fraction = 0.280.

run number normal raster currents	current μ A	carbon+lead singles $\times 10^7$	lead singles $\times 10^7$
1215	58	10.02	5.922
1216	51	10.01	5.909
1217	40	10.01	5.911
1225	45	9.959	5.857
1226	40	9.971	5.870
1227	41	9.983	5.882
1228	22	9.973	5.872
1229	39	10.02	5.920

Table 7.17: kin01-Normalized LHRS singles counts for the pb4 target. Normal raster currents. raster pattern from r1215 A(0.0004,-0.0022),B(0.0105,0.0065),cutsx(0.001,0.008),cutsy(0.0,0.005), visible hole in rastxy.

run number normal raster currents	current μ A	carbon+lead singles $\times 10^7$	lead singles $\times 10^7$
1233	50	10.14	6.042
1234	50	9.888	5.793
1235	46	9.906	5.811
1236	50	9.890	5.795
1237	48	9.875	5.780
1238	40	9.901	5.805
1239	42	9.870	5.774
1240	22	9.854	5.758
1259*	70	15.30	11.23
1260*	65	15.33	11.22

Table 7.18: kin02-Normalized LHRS singles counts for the pb4 target. Normal raster currents. raster pattern r1231, A(.00030,-.0022),B(.0105,.0065),cutsx(0.001,0.007),cutsy(-0.001,0.005). *raster pattern changed from r1255 onward, A(0.0048,0.0003),B(0.0215,0.0159),cutsx(0.007,0.020),cutsy(0.002,0.014).

7.3 Lead discussion

Lead target pb3 first saw beam from runs 1376 onward in kin04, table 7.5. The first few runs, 1376 to 1380, were low current runs from 0.9 to 9.7 μ A. I assume that the target did not deteriorate for these currents. A 3D plot of the reaction point is shown in figure 7.6. Assuming the pb3 target had the original thickness and accounting for the modest change in carbon content between graphite and the diamond sandwich it is possible to deduce the number of nuclei of heavy metal compared to carbon nuclei. Comparing runs 1339(carbon) to 1379 and 1380(pb3) the number density of pb nuclei is $\rho_{pb} = 6.51 \times 10^{20}/cm^2$ the carbon density in the sandwich is $\rho_c = 4.86 \times 10^{21}/cm^2$. Assuming the protons contribute the bulk of the electron interactions we can compare the proton densities from lead and carbon: $\rho_{pb}/\rho_c = 5.34 \times 10^{22}/2.91 \times 10^{22} = 1.84$. The normalized counting rate ratio for these runs is $cnts_{pb}/cnts_c = 9.073 \times 10^7/4.96 \times 10^7 = 1.83$. The ratios are encouragingly close considering they do not take into account any other nuclear effects. A geant simulation using the carbon singles spectrum as input produces the corresponding carbon spectrum from the lead target and takes into account radiative effects.

In tables 7.5 and 7.6 the normalized singles yields are displayed for two sizes of the raster cuts. The average yield in table 7.5 (9.07×10^7) is systematically smaller than in table 7.6 (9.11×10^7) by 0.5% and this may be due to either raster nonuniformity or target nonuniformity but this is much smaller than the 4% spread in the carbon yields. Near the end of the run for kin11 we see that the size of the raster cut in tables 7.15 and 7.16 makes a difference. The average yield in table 7.16 (9.81×10^7) is systematically smaller than in table 7.15 (10.48×10^7) by 6%. This lower yield is also indicated by the bluer shading in the 3D plot for kin11 in figure 7.4. Compare the target morphology in kin11 at

run number normal raster currents	current μ A	carbon+lead singles $\times 10^7$	lead singles $\times 10^7$
1507	9	1.007	0.7224
1508	9.4	1.002	0.7174
1509	20	1.001	0.7171
1510	39	0.9915	0.7071
1511	38	0.9969	0.7126

Table 7.19: kin12-Normalized LHRS singles counts for the pb3 target. Normal raster currents. raster pattern r1506, A(.006,0.0022),B(.0135,0.0104),cutsx(0.007,0.011),cutsy(0.004,0.009).

run number normal raster currents	current μ A	carbon+lead singles $\times 10^7$	lead singles $\times 10^7$
1494	10	0.2269	0.1810
1495	19	0.2257	0.1799
1496	39	0.2243	0.1785
1497	38	0.2258	0.1800
1498	36	0.2253	0.1795
1499	37	0.2247	0.1789
1500	36	0.2280	0.1822
1501	14	0.2266	0.1808

Table 7.20: kin13-Normalized LHRS singles counts for the pb3 target. Normal raster currents. raster pattern r1491, A(.006,0.0022),B(.0135,0.0104),cutsx(0.007,0.011),cutsy(0.004,0.009).

the end of the run to that in kin04 at the start of the run, figure 7.6.

Based on these discussions and equation 3.13 the effective lead target densities are calculated by equation 7.1

$$\frac{6.51 \times 10^{20}/cm^2}{9.073 \times 10^7/Coulomb_{eff}} = \frac{effective\ pb\ thickness}{yield/Coulomb_{eff}} \quad (7.1)$$

7.4 Kinematics 12 and 13

For kinematics 12 and 13 the LHRS was moved to new angles so the LHRS no longer can be used as a luminosity monitor. It is of interest, nevertheless, to compare the yields of the graphite target to the lead target. Table 7.19 shows the yield for kinematics 12 and table 7.20 is for kinematics 13.

Plots of the comparison of the normalized carbon and pb3 targets are shown in figures 7.7 and 7.8.

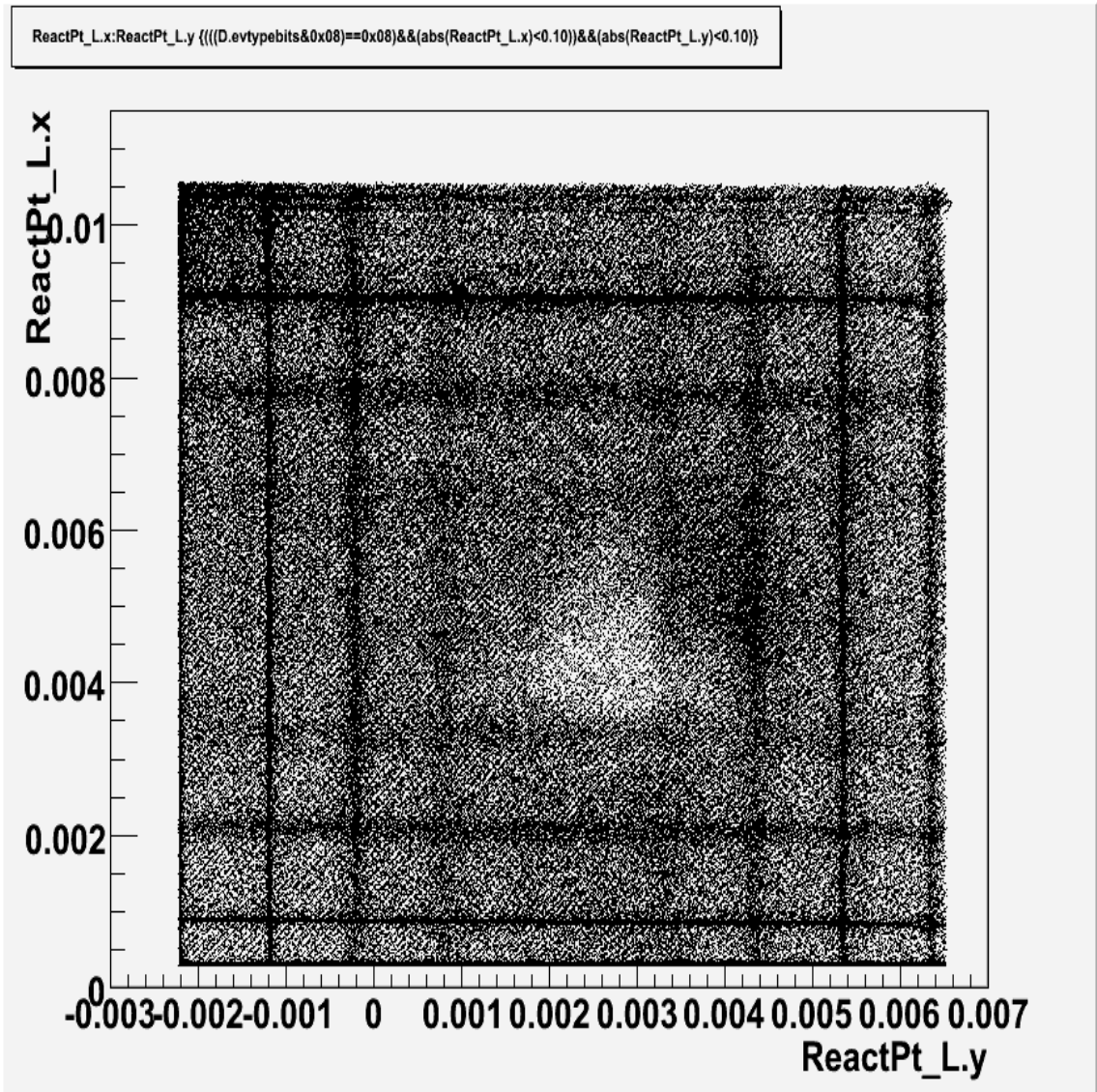


Figure 7.1: A plot of ReactPt.L.x vs ReactPt.L.y of the lead target4, run 1215, for the first run of kin01. Depletion of lead is already seen here.

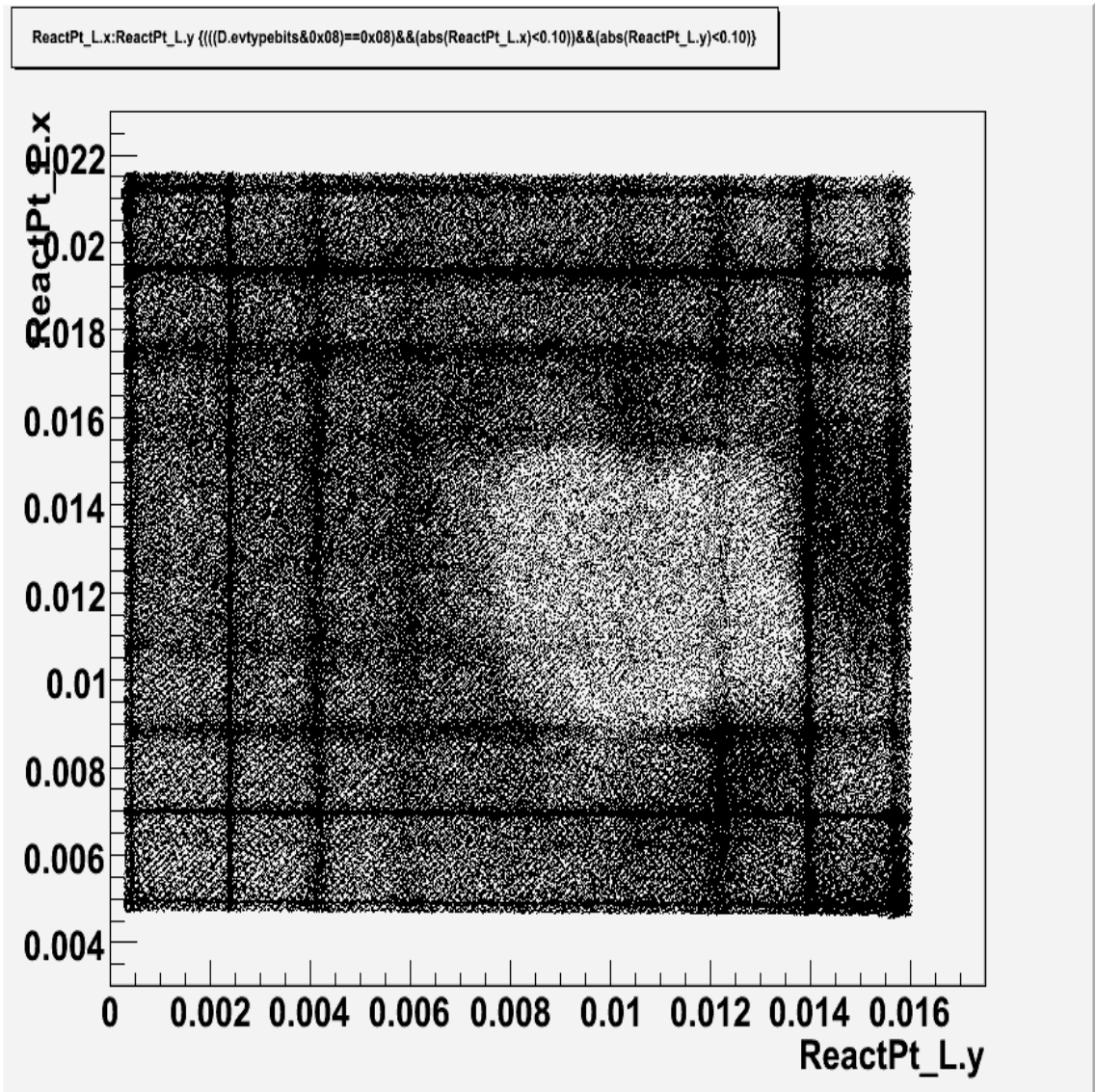


Figure 7.2: A plot of ReactPt.L.x vs ReactPt.L.y of the lead target4, run 1260, for kin02. The size of the depleted lead region is substantially larger than in figure 7.1.

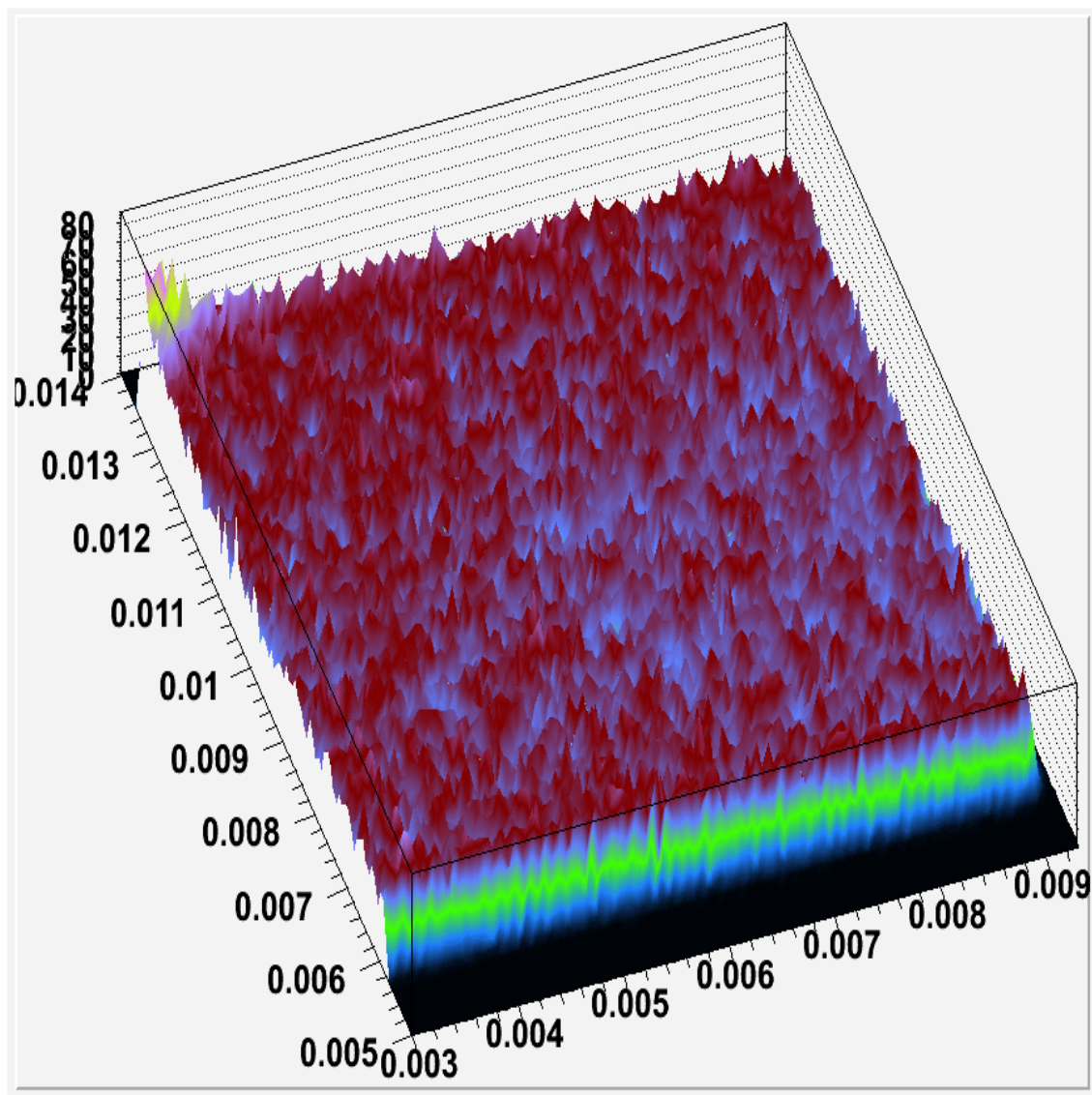


Figure 7.3: A 3 dimensional plot of ReactPt.L.x vs ReactPt.L.y of the lead target3, run 1585, for kin07.

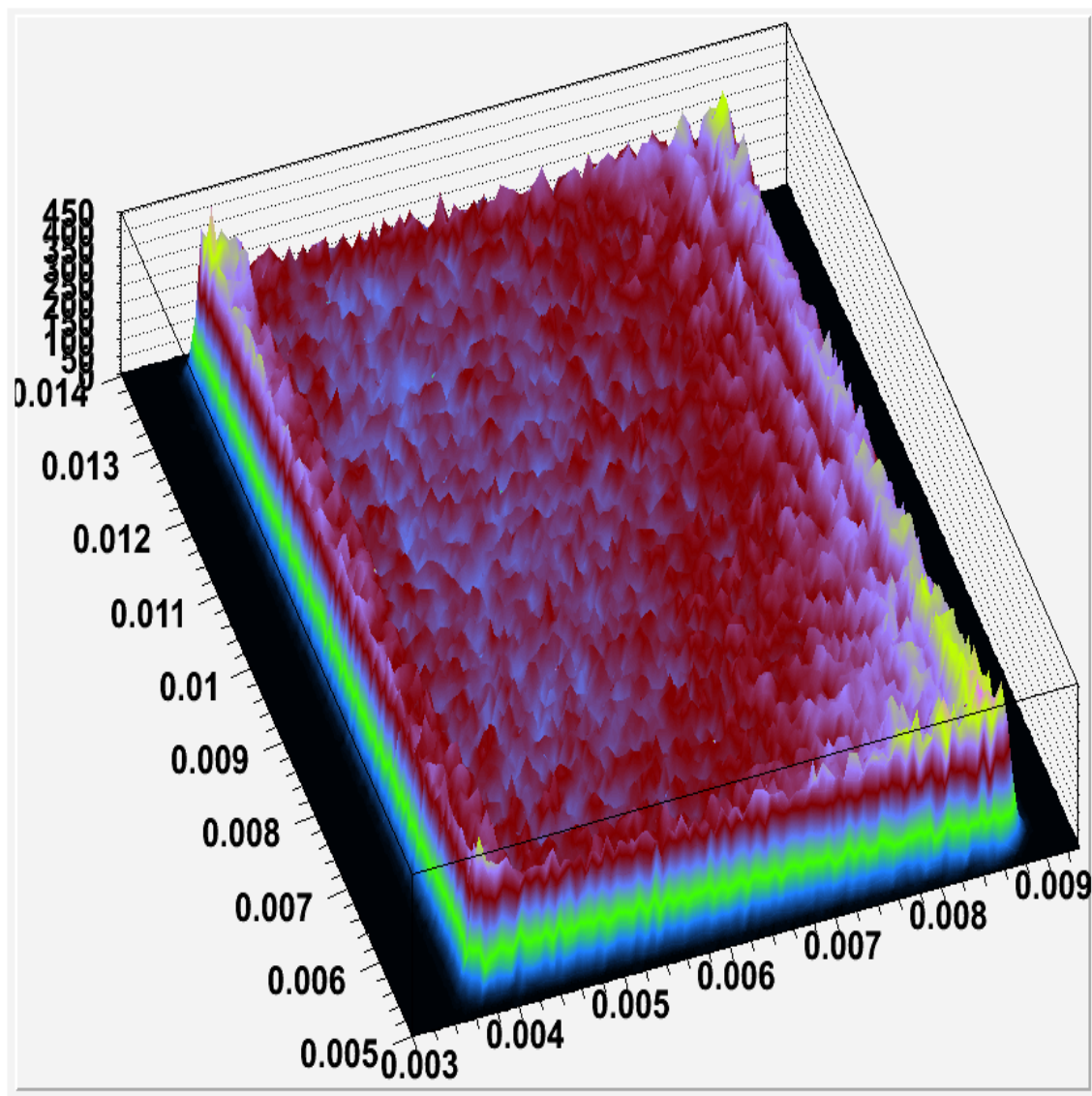


Figure 7.4: A 3 dimensional plot of ReactPt.L.x vs ReactPt.L.y of the lead target3, runs 1913,1914,1915 for kin11.

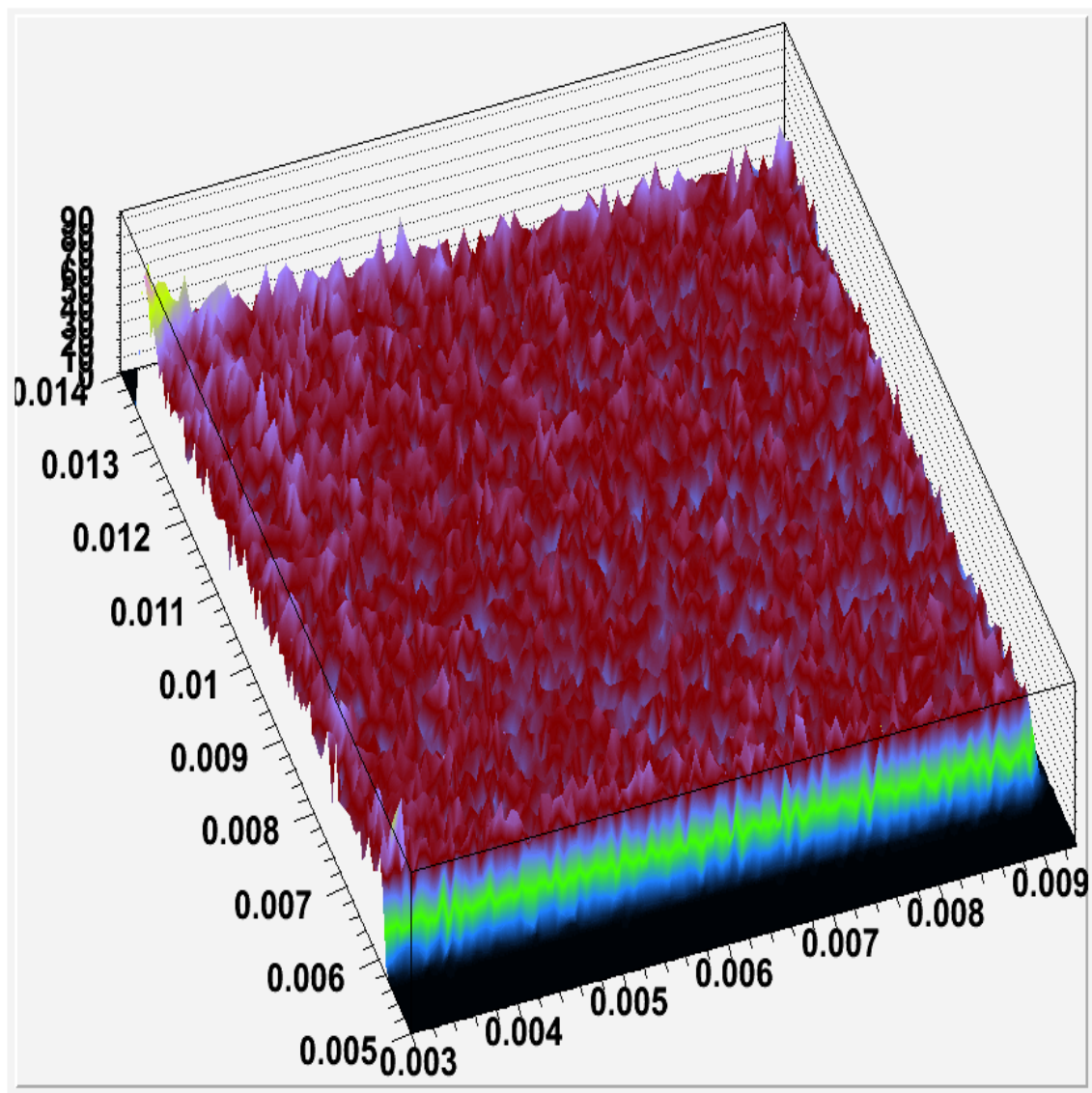


Figure 7.5: A 3 dimensional plot of ReactPt.L.x vs ReactPt.L.y of the lead target3, run 1609, for kin07.

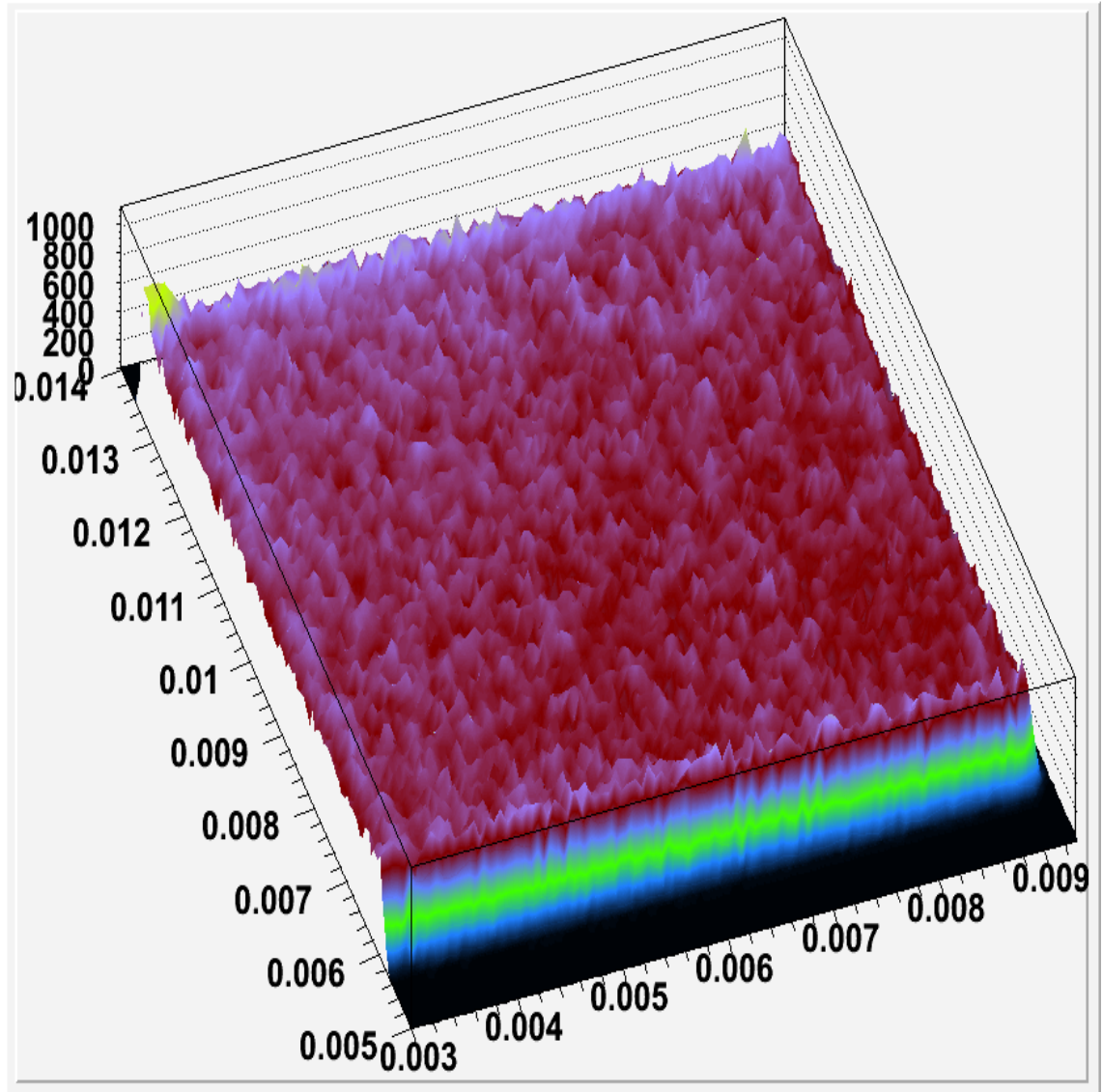


Figure 7.6: A 3 dimensional plot of ReactPt.L.x vs ReactPt.L.y of the lead target3, runs 1376 to 1380 for kin04. These are low current runs($I \leq 10\mu A$) taken when pb3 was first placed in the beam.

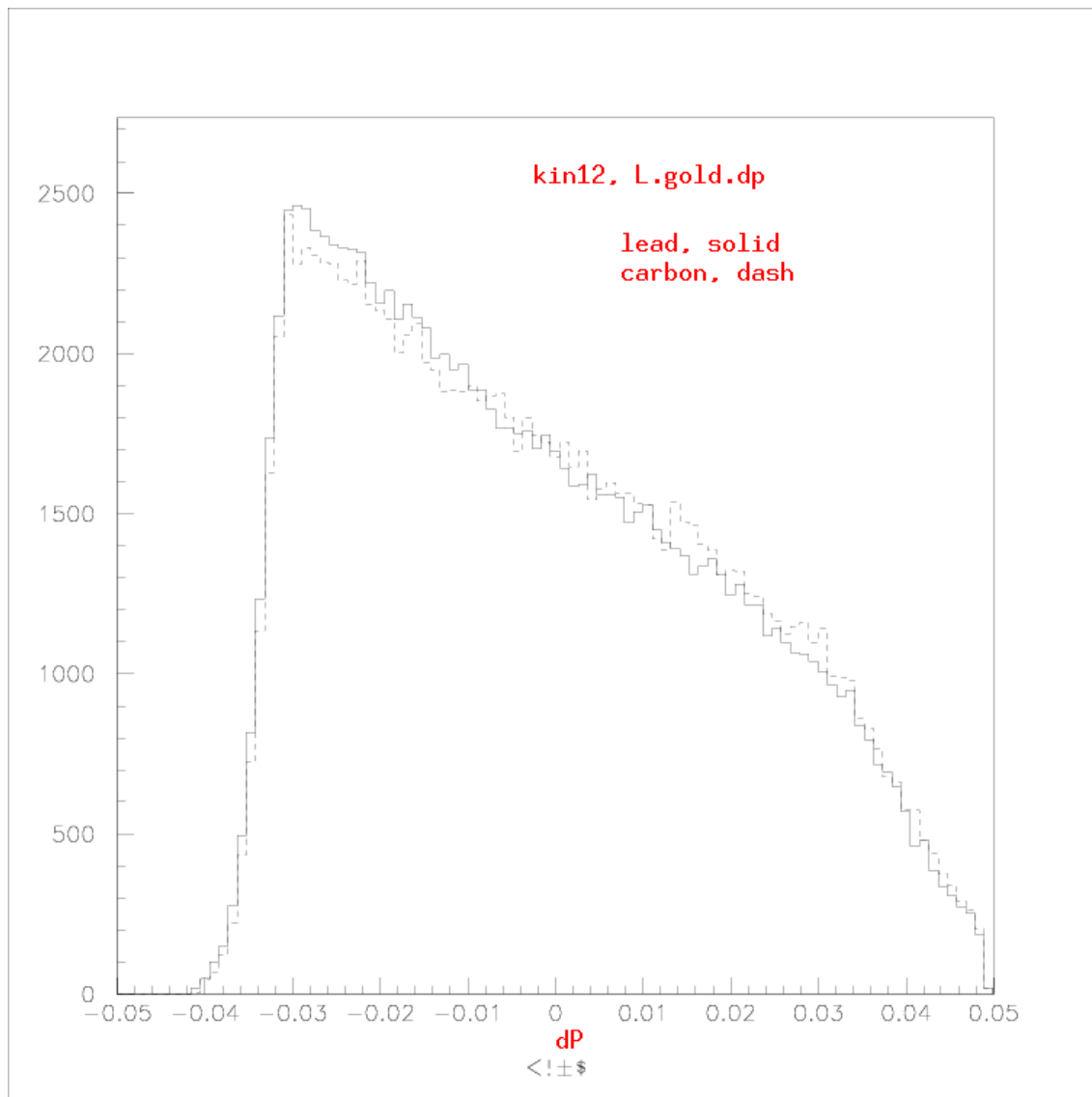


Figure 7.7: Measured L.gold.dp for kinematics 12. The spectra are normalized to have the same number of counts.

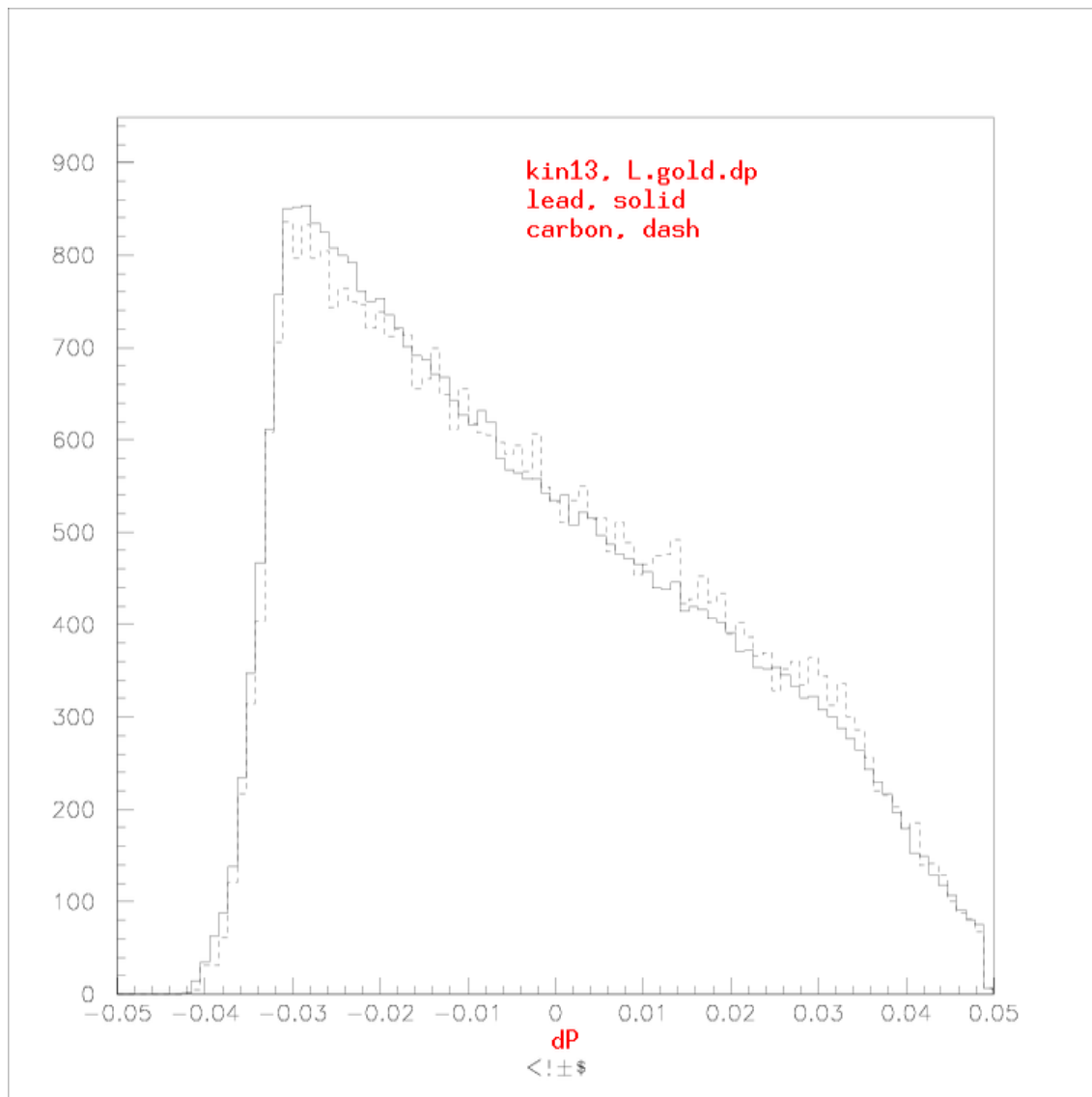


Figure 7.8: Measured L.gold.dp for kinematics 13. The spectra are normalized to have the same number of counts.

Chapter 8

Lead Results

8.1 Kinematics 1-11

Results for the effective thickness of the lead target, (pb3), gleaned from tables 7.1 to 7.15, are shown in table 8.1 for the case where radiative corrections are applied to the carbon singles spectrum and in table 8.3 where radiative corrections were not applied. The normalized yields differ but the final results for the effective thicknesses do not differ by more than 1%. The cuts in ReactPt.L.x and ReactPt.L.y are well within the raster pattern, never including more than about 50% of the whole current.

There is a general increase of the normalized singles yield with run number. A chronological history of the yield is seen in figure 8.1. This pattern of change is consistent with the changing morphology of the targets we see between the beginning of the run and the end of the run in figures 7.6 and 8.2. We also see a spike in yield around runs around 1600.

Target lead 4(pb4) can also be used for kinematics 01 and 02. The effective thickness for this target and these kinematics and raster cuts is shown in table 8.2 for the case of applying the radiative corrections and in table 8.4 where radiative corrections are not used.

8.2 Kinematics 12 and 13

Since we do not have a direct measurement of the lead content during kinematics 12 and 13 using the LHRS as a luminosity monitor it was investigated whether or not a simple model of graphite yield versus pb3 yield based on the atomic numbers of carbon and lead might be useful. We saw in the geant simulation, table 6.1, the radiative correction to subtract the carbon yield depends on the momentum and angle of the LHRS. A comparison of the $\text{yield(pb)}/\text{yield(c)}$ is presented in table 8.5. If the yield ratio were independent of LHRS angle and momentum then the simple model would give a ratio consistent with the result obtain for kin04, that is, $\text{yield(pb)}/\text{yield(c)}=1.83$, which agrees with the simple

kin	cutsx	cutsy	average yield $\times 10^7 / \text{Coulomb}$	normalization factor	effective thickness $\times 10^{20} / \text{cm}^2$
01	(0.007,0.011)	(0.003,0.009)	8.87 ± 0.01	1	6.37 ± 0.01
01*	(0.007,0.011)	(0.003,0.009)	8.20 ± 0.01	0.95	6.27 ± 0.01
02*	(0.007,0.011)	(0.004,0.009)	9.28 ± 0.01	0.95	6.33 ± 0.01
03*	(0.007,0.011)	(0.003,0.009)	9.33 ± 0.05	0.95	6.36 ± 0.04
04	(0.006,0.012)	(0.004,0.009)	9.07 ± 0.03	1	6.51 ± 0.02
04	(0.009,0.012)	(0.004,0.009)	9.11 ± 0.08	1	6.54 ± 0.06
04*	(0.007,0.012)	(0.0045,0.008)	10.2 ± 0.2	0.95	6.96 ± 0.15
05	(0.007,0.012)	(0.004,0.009)	9.34 ± 0.03	1	6.71 ± 0.02
05*	(0.007,0.012)	(0.004,0.009)	9.31 ± 0.04	0.95	6.35 ± 0.03
06	(0.006,0.012)	(0.004,0.009)	8.80 ± 0.03	1	6.32 ± 0.02
06*	(0.007,0.012)	(0.0045,0.0075)	10.6 ± 0.3	0.95	7.24 ± 0.23
07a	(0.007,0.011)	(0.003,0.009)	9.02 ± 0.07	1	6.47 ± 0.06
07b	(0.007,0.011)	(0.003,0.009)	9.48 ± 0.07	1	6.80 ± 0.06
08*	(0.007,0.011)	(0.004,0.009)	9.21 ± 0.06	0.95	6.28 ± 0.05
09a*	(0.007,0.013)	(0.0045,0.008)	9.62 ± 0.04	0.95	6.56 ± 0.03
09b*	(0.007,0.013)	(0.0045,0.008)	10.26 ± 0.07	0.95	7.00 ± 0.05
09c*	(0.007,0.013)	(0.0045,0.008)	10.55 ± 0.03	0.95	7.20 ± 0.02
10*	(0.007,0.012)	(0.004,0.008)	9.54 ± 0.15	0.95	6.50 ± 0.11
11*	(0.007,0.013)	(0.0045,0.008)	10.48 ± 0.45	0.95	7.15 ± 0.34
11*	(0.007,0.013)	(0.0065,0.008)	9.81 ± 0.40	0.95	6.69 ± 0.30

Table 8.1: Effective target thicknesses based on LHRS singles yields. Radiative corrections have been applied to the carbon subtracted spectrum. The effective thickness is determined from the average yield using equation 7.1. A * indicates reversed raster currents. Raster changed between kin07a and kin07b, see table 7.11. Raster changed during kin09a,b,c, see table 7.13.

kin	cutsx	cutsy	average yield $\times 10^7 / \text{Coulomb}$	normalization factor	effective thickness $\times 10^{20} / \text{cm}^2$
01	(0.001,0.008)	(0.0,0.005)	5.89 ± 0.02	1	4.23 ± 0.02
02a	(0.001,0.007)	(-0.001,0.005)	5.82 ± 0.02	1	4.18 ± 0.02
02b	(0.007,0.020)	(0.002,0.014)	11.2 ± 0.1	1	8.06 ± 0.08

Table 8.2: Target Pb4. Effective target thicknesses based on LHRS singles yields. Radiative corrections have been applied to the carbon subtracted spectrum. The effective thickness is determined from the average yield using equation 7.1. Raster changed between kin02a and kin02b, see table 7.18.

kin	cutsx	cutsy	average yield $\times 10^7 / \text{Coulomb}$	normalization factor	effective thickness $\times 10^{20} / \text{cm}^2$
01	(0.007,0.011)	(0.003,0.009)	7.933 ± 0.002	1	6.31 ± 0.01
01*	(0.007,0.011)	(0.003,0.009)	8.32 ± 0.01	0.95	6.29 ± 0.01
02*	(0.007,0.011)	(0.004,0.009)	8.36 ± 0.01	0.95	6.32 ± 0.01
03*	(0.007,0.011)	(0.003,0.009)	8.41 ± 0.05	0.95	6.36 ± 0.04
04	(0.006,0.012)	(0.004,0.009)	8.18 ± 0.03	1	6.51 ± 0.02
04	(0.009,0.012)	(0.004,0.009)	8.24 ± 0.08	1	6.56 ± 0.06
04*	(0.007,0.012)	(0.0045,0.008)	9.29 ± 0.2	0.95	7.03 ± 0.15
05	(0.007,0.012)	(0.004,0.009)	8.43 ± 0.03	1	6.71 ± 0.02
05*	(0.007,0.012)	(0.004,0.009)	8.40 ± 0.04	0.95	6.35 ± 0.03
06	(0.006,0.012)	(0.004,0.009)	7.93 ± 0.03	1	6.31 ± 0.02
06*	(0.007,0.012)	(0.0045,0.0075)	9.7 ± 0.3	0.95	7.34 ± 0.23
07a	(0.007,0.011)	(0.003,0.009)	8.13 ± 0.07	1	6.47 ± 0.06
07b	(0.007,0.011)	(0.003,0.009)	8.59 ± 0.07	1	6.84 ± 0.06
08*	(0.007,0.011)	(0.004,0.009)	8.36 ± 0.06	0.95	6.32 ± 0.05
09a*	(0.007,0.013)	(0.0045,0.008)	8.68 ± 0.04	0.95	6.56 ± 0.03
09b*	(0.007,0.013)	(0.0045,0.008)	9.33 ± 0.07	0.95	7.06 ± 0.05
09c*	(0.007,0.013)	(0.0045,0.008)	9.61 ± 0.03	0.95	7.27 ± 0.02
10*	(0.007,0.012)	(0.004,0.008)	8.60 ± 0.15	0.95	6.50 ± 0.11
11*	(0.007,0.013)	(0.0045,0.008)	9.54 ± 0.45	0.95	7.21 ± 0.34
11*	(0.007,0.013)	(0.0065,0.008)	8.87 ± 0.40	0.95	6.71 ± 0.30

Table 8.3: Effective target thicknesses based on LHRS singles yields. No radiative correction to the carbon subtracted spectrum have been applied. The effective thickness is determined from the average yield using equation 7.1 with the normalization yield = 8.177×10^7 . A * indicates reversed raster currents. Raster changed between kin07a and kin07b, see table 7.11. Raster changed during kin09a,b,c, see table 7.13.

kin	cutsx	cutsy	average yield $\times 10^7 / \text{Coulomb}$	normalization factor	effective thickness $\times 10^{20} / \text{cm}^2$
01	(0.001,0.008)	(0.0,0.005)	4.99	1	3.97 ± 0.02
02a	(0.001,0.007)	(-0.001,0.005)	4.92	1	3.92 ± 0.06
02b	(0.007,0.020)	(0.002,0.014)	10.32	1	8.21 ± 0.01

Table 8.4: Target Pb4. Effective target thicknesses based on LHRS singles yields. No radiative correction to the carbon subtracted spectrum have been applied. The effective thickness is determined from the average yield using equation 7.1 with the normalization yield = 8.177×10^7 .. Raster changed between kin02a and kin02b, see table 7.18.

	kin04	kin12	kin13
$p_0(GeV/c)$	2.216	1.902	1.602
$\theta_L(\text{deg})$	21.44	30.59	39.72
yield(pb)/yield(c)	1.83	1.91	2.58

Table 8.5: The ratio yield(pb)/yield(c) for momenta and angles for the LHRS.

model. From table 8.5 it is evident that this model does not work for kin12 or kin13. Perhaps the agreement with kin04 is fortuitous. However, it is reasonable to use a target density of $6.33 \pm 0.03 \times 10^{20}/cm^2$ for kinematics 12 and 13. This density comes from table 8.1. The runs for kin06(1434-1486) and kin01(1512-1517) sandwich the runs for kin12(1507-1511) and kin13(1494-1501) and from table 8.1 the density is constant.

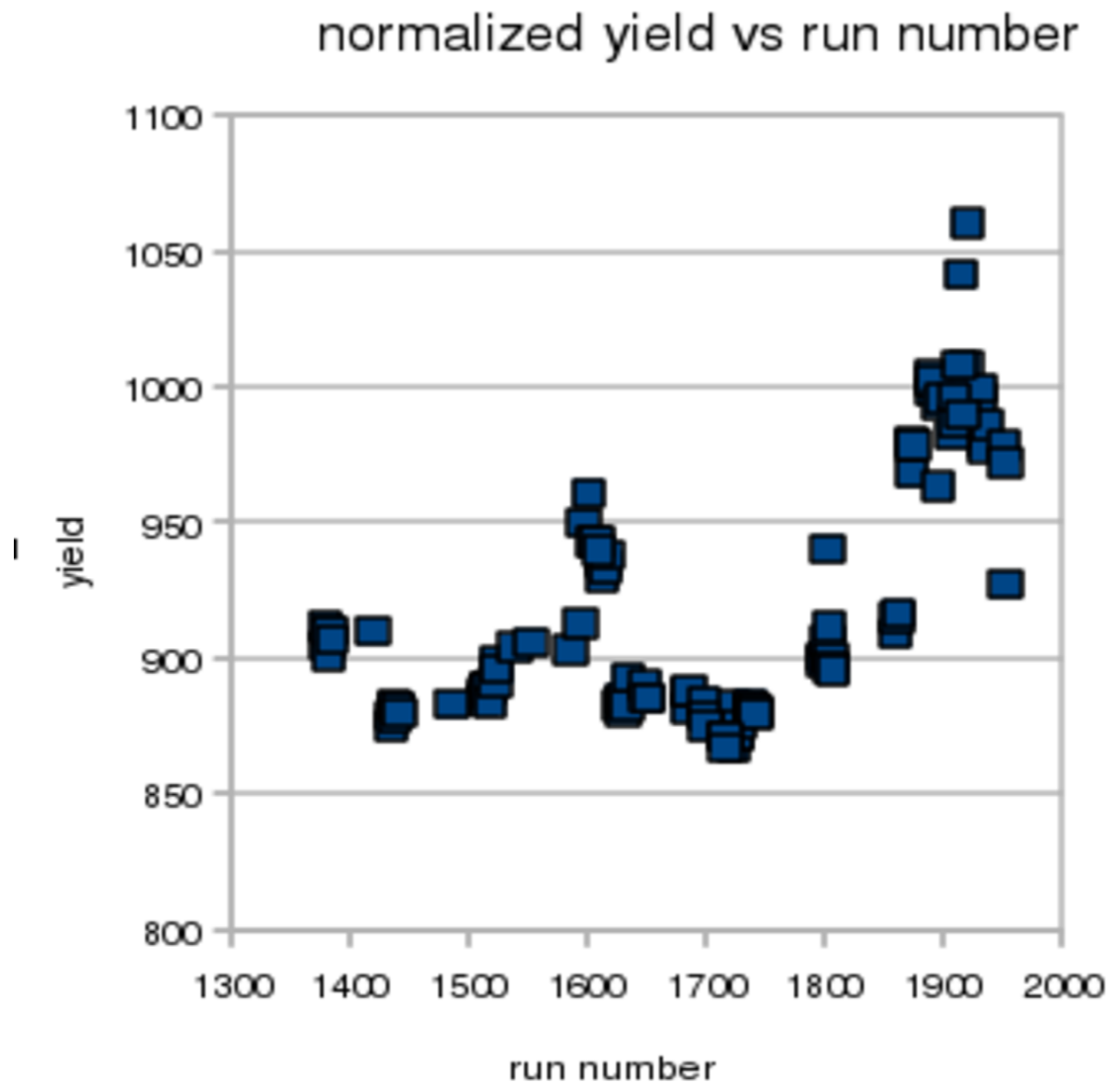


Figure 8.1: Normalized yield vs run number. The vertical scale should be multiplied by 10^5 .

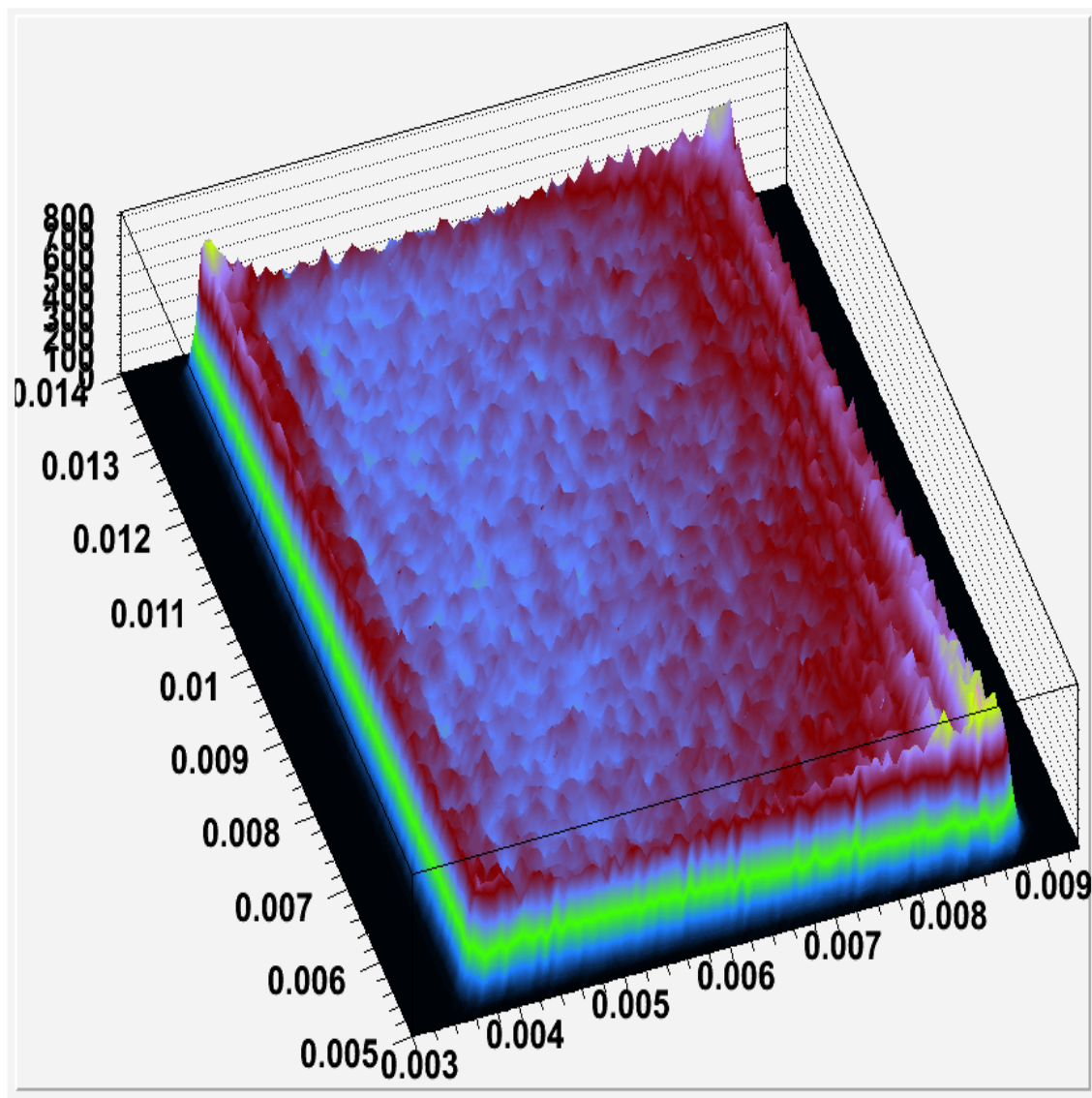


Figure 8.2: 3D raster yield plot for runs 1928,1929,1930.

Chapter 9

Bismuth data

9.1 Bismuth Data

The bismuth target for run 1 was damaged. In figures 9.1 and 9.2 we see the uneven morphology of the bismuth targets. By normalizing the singles spectrum we should be able to determine the absolute numbers of bismuth nuclei in the beam. Since the morphology of the target may change with time and the numbers of target nuclei in the electron beam depends on the raster cut there may well be a change in the normalized singles rates for the heavy metal targets. Note the raster current leads or adc inputs were switched between figure 9.1 and figure 9.2.

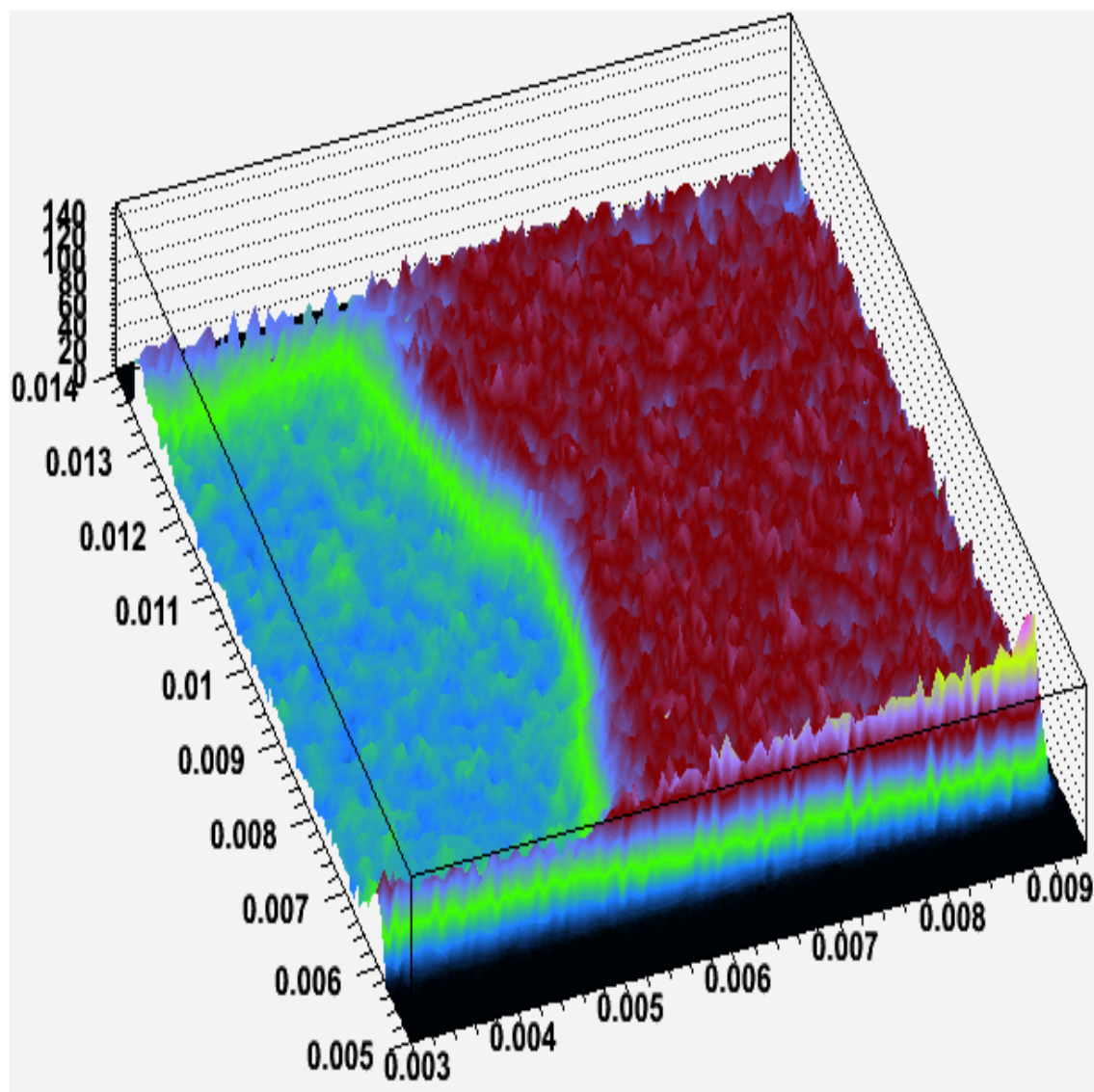


Figure 9.1: A 3 dimensional plot of ReactPt_L.x vs ReactPt_L.y of the bismuth target, run 1360, for kin04 showing the ragged topology of the metal surface and the bare diamond substrate.

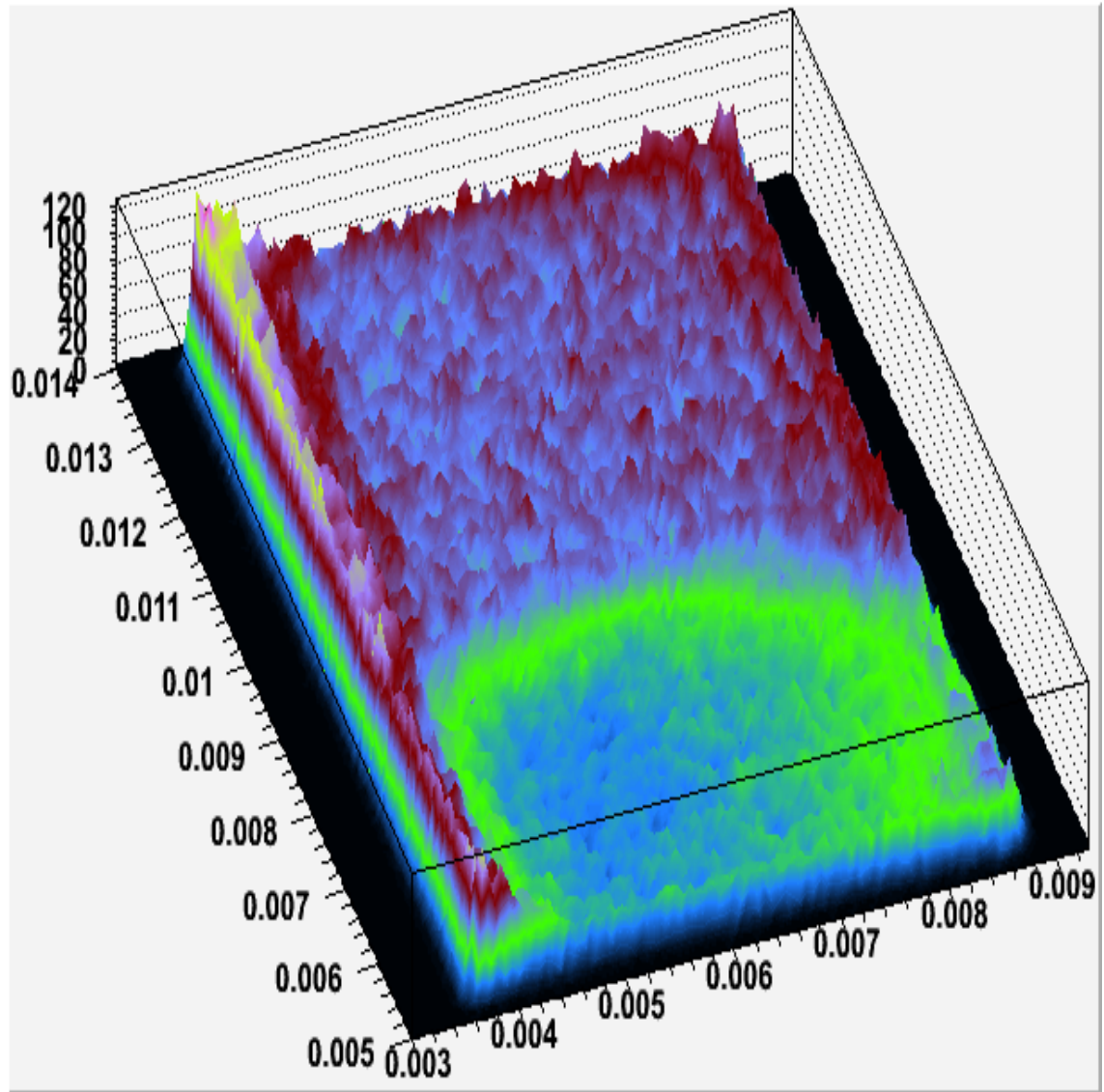


Figure 9.2: A 3 dimensional plot of ReactPt_L.x vs ReactPt_L.y of the bismuth target, run 1960, for kin04 showing the ragged topology of the metal surface and the bare diamond substrate. The raster current leads were accidentally switched.

run number normal raster currents	current μ A	carbon+lead singles $\times 10^7$	lead singles $\times 10^7$
1326	68	18.32	13.81
1327	47	18.36	13.86
1328	40	18.58	14.08

Table 9.1: kin02-Normalized LHRS singles counts for the bismuth target. Normal raster currents. raster pattern r1326, A(.0051,.003),B(.0143,.0095), cutsx(.006,.013),cutsy(.006,.0085)

run number reverse raster currents	current μ A	carbon+lead singles $\times 10^7$	lead singles $\times 10^7$
1977*	37	19.32	14.57
1978*	35	19.22	14.52
1979*	36	19.32	14.61
1980*	33	19.28	14.57
1981*	36	19.29	14.58
1982*	38	19.26	14.55

Table 9.2: kin03-Normalized LHRS singles counts for the bismuth target. Reverse raster currents. raster pattern r1977, A(.0055,.0037),B(.0140,.0088), cutsx(.0095,.013),cutsy(.005,.008)

9.2 Bismuth Results

The effective target thickness for the bismuth target is displayed in table 9.8 for the case where radiative corrections are applied to the subtracted carbon spectrum. The effective target thickness for the bismuth target is displayed in table 9.9 for the case where radiative corrections are not applied to the subtracted carbon spectrum. The bismuth target is distinctly thicker than the lead target and the original thickness of the bismuth foil ($5.90 \times 10^{20}/cm^2$). This can possibly be explained by assuming that the bismuth target melted during the Iscan runs (March 9, 2007, hall A logbook entry 195299) and bismuth flowed building up a thicker region. The Iscan did not reveal any suspicious behavior for the target, the total rate for trig3 being linearly proportional to the current, figure 9.5. Nevertheless, it was noted that the bismuth rate was larger than the rate from the lead target by a factor of 1.47. This suggests that the bismuth flowed into the beam region from regions that were outside the beam, rather than simply rearranging the amount of bismuth initially under the beam. The first few 80000 events of run 1326 were investigated with the hope that the bismuth foil would not have melted so early on. However, the foil already shows signs of damage (figure 9.4). The 3D plot for the entire run 1326 is seen in figure 9.3.

run number normal raster currents	current μ A	carbon+lead singles $\times 10^7$	lead singles $\times 10^7$
1360	35	18.16	13.59
1353	23	18.17	13.60
1354	32	18.13	13.56
1355	28	18.14	13.57
1370	38	18.27	13.69
1372	36	18.26	13.68
1373	30	18.25	13.68
1374	35	18.16	13.59
1375	36	18.19	13.61

Table 9.3: kin04-Normalized LHRS singles counts for the bismuth target. Normal raster currents. raster pattern r1360, A(.006,.0022),B(.0134,.0102),cutsx(.007,.012),cutsy(.006,.009)

run number reverse raster currents	current μ A	carbon+lead singles $\times 10^7$	lead singles $\times 10^7$
1960*	38	19.75	15.04
1956*	31	19.93	15.22
1957*	36	19.90	15.19
1958*	36	19.98	15.27
1973*	36	20.31	15.60
1974*	37	20.19	15.47
1975*	36	20.13	15.42
1976*	37	20.20	15.49

Table 9.4: kin04-Normalized LHRS singles counts for the bismuth target. Reverse raster currents. raster pattern r1960, A(.0054,.0037),B(.0140,.0088),cutsx(.009,.013),cutsy(.005,.008)

run number reverse raster currents	current μ A	carbon+lead singles $\times 10^7$	lead singles $\times 10^7$
1985*	30	19.52	14.81
1986*	37	19.76	15.05
1987*	36	19.38	14.67
1993*	36	19.42	14.70
1994*	40	19.49	14.78
1995*	36	19.34	14.63
2002*	36	19.54	14.83
2003*	35	19.32	14.61
2004*	36	19.56	14.85

Table 9.5: kin05-Normalized LHRS singles counts for the bismuth target. Reverse raster currents. raster pattern r1985 A(0.0055,0.0037),B(0.014,0.0088),cutsx(0.01,0.013),cutsy(0.005,0.008).

run number normal raster currents	current μ A	carbon+lead singles $\times 10^7$	lead singles $\times 10^7$
1422	36	17.56	13.09
1423	36	17.64	13.17
1424	36	17.60	13.13
1425	37	17.46	13.00
1426	36	17.54	13.07
1427	37	17.54	13.07
1428	38	17.54	13.07
1429	37	17.64	13.17
1430	38	17.61	13.14
1431	37	17.61	13.14
1432	35	17.65	13.18
1433	15	17.66	13.19

Table 9.6: kin06-Normalized LHRS singles counts for the bismuth target. normal raster currents. raster pattern. r1422, A(0.006,0.0023), B(0.0135,0.010),cutsx(0.007,0.012),cutsy(0.006,0.009).

run number reverse raster currents	current μ A	carbon+lead singles $\times 10^7$	lead singles $\times 10^7$
2005*	10	18.45	13.74
2006*	19	18.69	13.98
2007*	35	19.37	14.66
2008*	36	19.37	14.66
2009*	24	19.35	14.64
2010*	36	19.48	14.77
2011*	34	19.33	14.62
2012*	38	19.44	14.73
2013*	36	19.42	14.71
2014*	13	19.46	14.75

Table 9.7: kin07-Normalized LHRS singles counts for the bismuth target. reverse raster currents. raster pattern. r2008 A(0.0055,0.0037),B(0.014,0.0088),cutsx(0.01,0.013),cutsy(0.005,0.008).

kin	cutsx	cutsy	average yield $\times 10^7 / \text{Coulomb}$	normalization factor	effective thickness $\times 10^{20} / \text{cm}^2$
02	(0.006,0.013)	(0.006,0.0085)	13.92 ± 0.14	1	10.26 ± 0.11
03*	(0.0095,0.013)	(0.005,0.008)	14.57 ± 0.01	0.95	10.21 ± 0.01
04	(0.007,0.012)	(0.006,0.009)	13.62 ± 0.05	1	10.05 ± 0.04
04*	(0.009,0.013)	(0.005,0.008)	15.3 ± 0.2	0.95	10.75 ± 0.15
05*	(0.01,0.013)	(0.005,0.008)	14.77 ± 0.14	0.95	10.35 ± 0.1
06	(0.007,0.012)	(0.006,0.009)	13.12 ± 0.1	1	9.68 ± 0.08
07*	(0.01,0.013)	(0.005,0.008)	14.5 ± 0.4	0.95	10.18 ± 0.3

Table 9.8: Bismuth effective target thicknesses based on LHRS singles yields. Radiative corrections to the subtracted carbon spectrum have been applied. The effective thickness is determined from the average yield using equation 7.1. A * indicates reversed raster currents. The bismuth effective thickness includes an additional factor of 82/83 to account for the extra proton in bismuth compared to lead and a factor of 1.04 to account for radiative differences.

kin	cutsx	cutsy	average yield $\times 10^7 / \text{Coulomb}$	normalization factor	effective thickness $\times 10^{20} / \text{cm}^2$
02	(0.006,0.013)	(0.006,0.0085)	12.93 ± 0.14	1	10.17 ± 0.11
03*	(0.0095,0.013)	(0.005,0.008)	13.54 ± 0.01	0.95	10.12 ± 0.01
04	(0.007,0.012)	(0.006,0.009)	12.62 ± 0.05	1	9.92 ± 0.04
04*	(0.009,0.013)	(0.005,0.008)	14.3 ± 0.2	0.95	10.68 ± 0.15
05*	(0.01,0.013)	(0.005,0.008)	13.74 ± 0.14	0.95	10.27 ± 0.1
06	(0.007,0.012)	(0.006,0.009)	12.14 ± 0.1	1	9.55 ± 0.08
07*	(0.01,0.013)	(0.005,0.008)	13.5 ± 0.4	0.95	10.09 ± 0.3

Table 9.9: Bismuth effective target thicknesses based on LHRS singles yields. No radiative corrections to the subtracted carbon spectrum have been applied. The effective thickness is determined from the average yield using equation 7.1 for a normalization factor of 8.177×10^7 . A * indicates reversed raster currents. The bismuth effective thickness includes an additional factor of 82/83 to account for the extra proton in bismuth compared to lead.

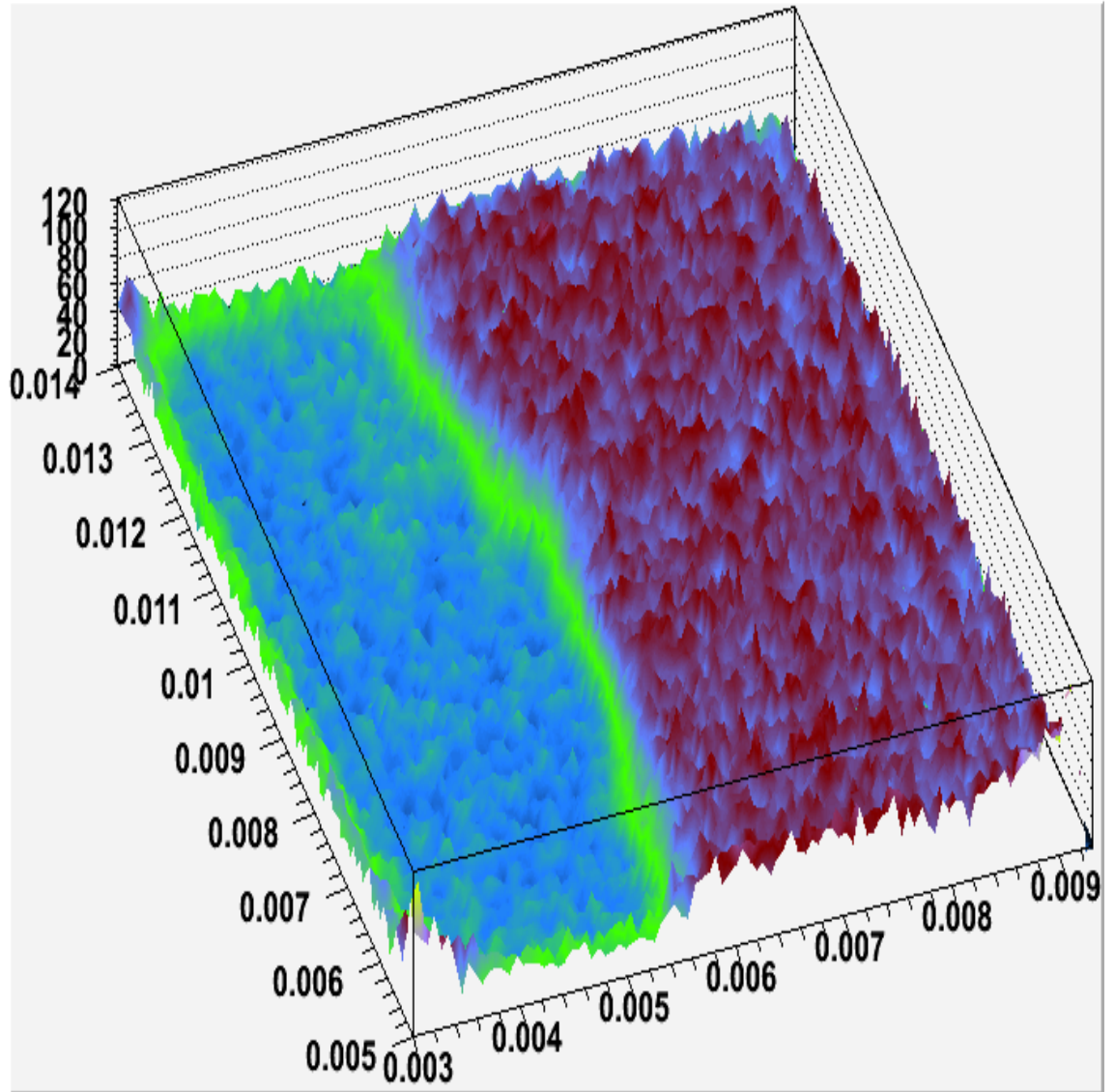


Figure 9.3: A 3 dimensional plot of ReactPt.L.x vs ReactPt.L.y of the bismuth target, run 1326.

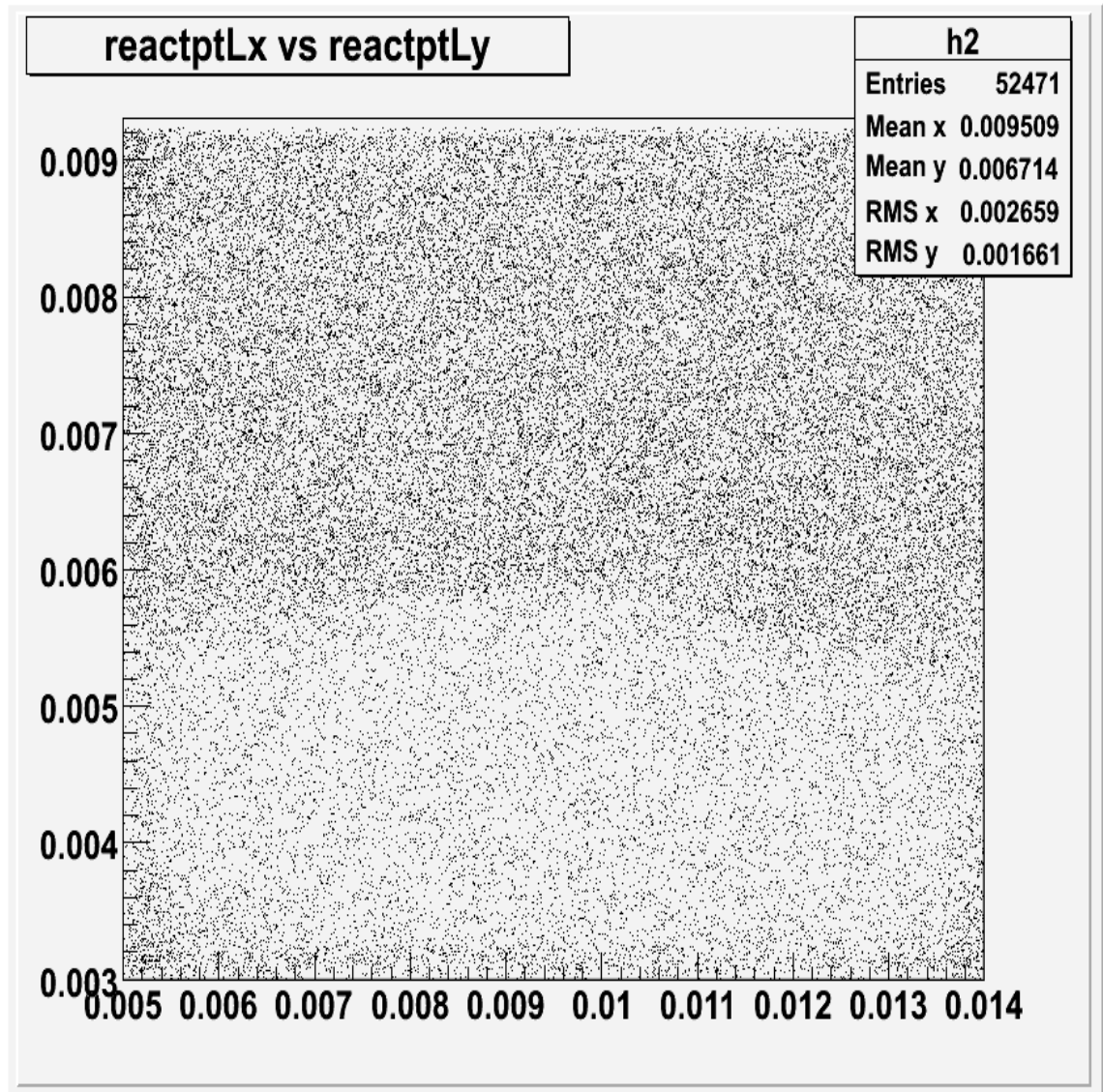


Figure 9.4: A plot of ReactPt.L.x vs ReactPt.L.y of the bismuth target, for the first 80000 events of run 1326. This is the first run of kin02. The damage to the target is already evident. The target started out damaged, probably during the Iscan runs.

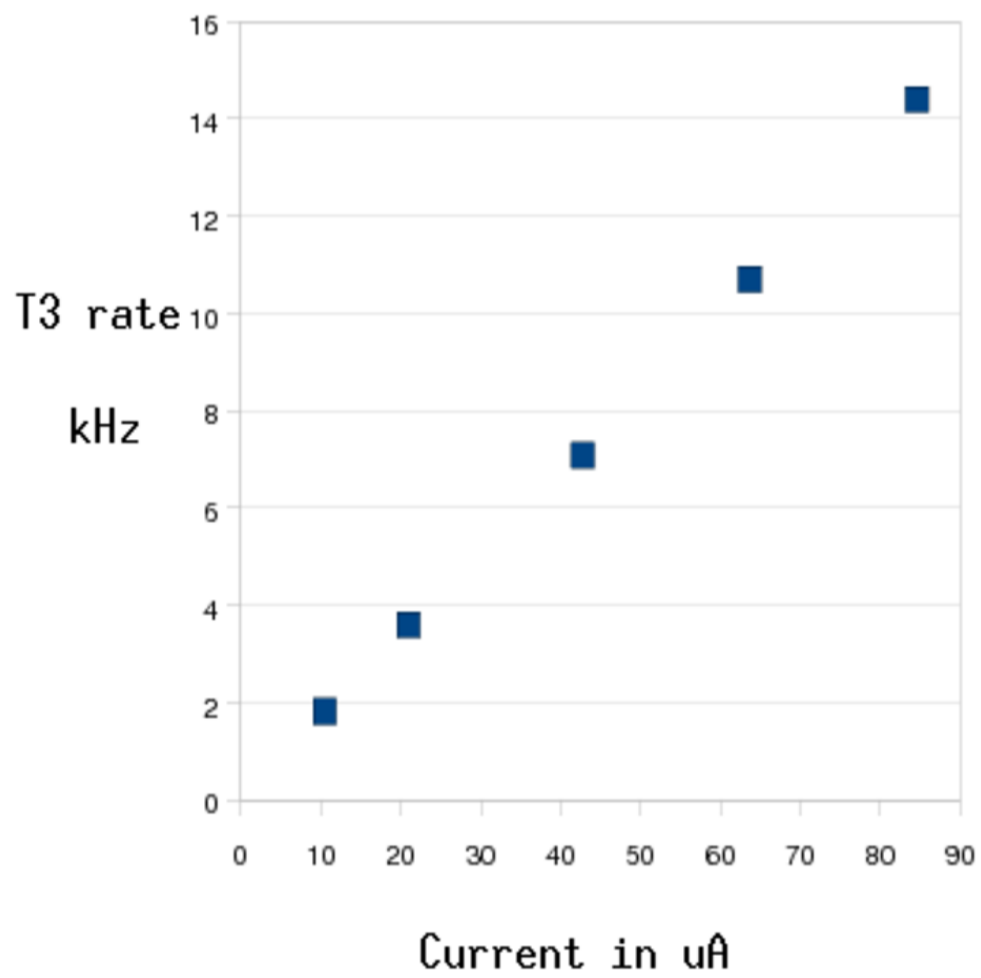


Figure 9.5: A plot of trigger 3 rate versus current for the bismuth target taken prior to run 1326 during the Iscan run, hall A logbook entry 195299, March 9, 2007.